END
DATE
FILMED
4-83
DTIC
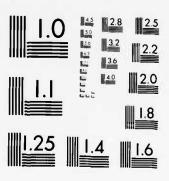
MICROCOPY RESOLUTION TEST CHART

NATIONAL BUREAU OF STANDARDS-1963-A

RADC-TR-82-311
Final Technical Report
December 1982

GRATING BEAM COMBINER

Itek Corporation

Sponsored by
Defense Advanced Research Projects Agency (DOD)
ARPA Order No. 3503

APPROVED FOR PUBLIC RELEASE; DISTRIBUTION UNLIMITED

ROME AIR DEVELOPMENT CENTER
Air Force Systems Command
Griffiss Air Force Base, NY 13441

83 03 09 006

This report has been reviewed by the RADC Public Affairs Office (PA) and is releasable to the National Technical Information Service (NTIS). At NTIS it will be releasable to the general public, including foreign nations.

RADC-TR-82-311 has been reviewed and is approved for publication.

APPROVED: *(signature)*

JAMES W. CUSACK
Project Engineer

APPROVED: *(signature)*

FRANK J. REHM, Technical Director
Surveillance Division

FOR THE COMMANDER: *(signature)*

JOHN P. HUSS
Acting Chief, Plans Office

GRATING BEAM COMBINER

Michael E. Schroeder
Kenneth D. Stumpf
Mary A. Mullahy

REPORT DOCUMENTATION PAGE		READ INSTRUCTIONS BEFORE COMPLETING FORM
1. REPORT NUMBER RADC-TR-82-311	2. GOVT ACCESSION NO.	3. RECIPIENT'S CATALOG NUMBER
4. TITLE (and Subtitle) GRATING BEAM COMBINER		5. TYPE OF REPORT & PERIOD COVERED Final Technical Report July 80 – Sep 82
		6. PERFORMING ORG. REPORT NUMBER 82-152
7. AUTHOR(s) Michael E. Schroeder Kenneth D. Stumpf Mary A. Mullahy		8. CONTRACT OR GRANT NUMBER(s) F30602-80-C-0241
9. PERFORMING ORGANIZATION NAME AND ADDRESS Defense Advanced Research Projects Agency 1400 Wilson Blvd Arlington VA 02209		10. PROGRAM ELEMENT, PROJECT, TASK AREA & WORK UNIT NUMBERS 62711E C5030107
11. CONTROLLING OFFICE NAME AND ADDRESS Itek Corporation 10 Maguire Road Lexington MA 02173		12. REPORT DATE December 1982
		13. NUMBER OF PAGES 82
14. MONITORING AGENCY NAME & ADDRESS(if different from Controlling Office) Rome Air Development Center (OCSE) Griffiss AFB NY 13441		15. SECURITY CLASS. (of this report) UNCLASSIFIED
		15a. DECLASSIFICATION/DOWNGRADING SCHEDULE N/A

16. DISTRIBUTION STATEMENT (of this Report)

Approved for public release; distribution unlimited

17. DISTRIBUTION STATEMENT (of the abstract entered in Block 20, if different from Report)

Same

18. SUPPLEMENTARY NOTES

RADC Project Engineer: James W. Cusack (OCSE)

19. KEY WORDS (Continue on reverse side if necessary and identify by block number)

Beam sampling
gratings
beam control
aperture sharing components
diffraction gratings

high-energy lasers
Large Optics Demonstration
  Experiment (LODE)

20. ABSTRACT (Continue on reverse side if necessary and identify by block number)

The fabrication, test, and analysis of a two-wave length dual-frequency beam sampling grating have been performed. Measurements of the efficiency, diffracted wavefront quality, frequency ratio, and skew are described. Analysis of the effects of nonzero skew and frequency ratio residual on its performance are presented, as well as the required process tolerances to achieve acceptably low levels of each. A laboratory demonstration confirmed the invariance of the co-boresighting of the two wavelengths with respect

DD FORM 1473 1 JAN 73   EDITION OF 1 NOV 65 IS OBSOLETE

SUMMARY

The objective of this effort was to demonstrate the fabrication, characterization, and boresighting capabilities of a unique beam sampling component known as the Grating Beam Combiner (GBC). The concept is a significant alternative to the full-aperture holographic sampler. It diffracts samples of an outgoing high-energy infrared (IR) beam and an incoming designator beam in the same direction independent of angle of incidence on the grating.

Two samples of the proposed component were produced and characterized. In addition, a higher efficiency sample was produced and used for a laboratory demonstration of the unique sampling and boresighting properties of the GBC.

The characterization task included not only conventional grating parameters, such as groove depth and diffracted wavefront quality, but also addressed measurement of skew between the two component grating frequencies and their actual ratio.

Analysis of the GBC treats the sensitivity of its performance to skew and frequency ratio residuals. Specific requirements for the holographic pattern generation process to achieve small residuals are discussed.

The GBC has been successfully demonstrated and appears to be a viable candidate for generic two-wavelength beam sampling requirements.

iii

CONTENTS

FIGURES

TABLES

1. INTRODUCTION

Accurate beam control is a fundamental requirement on all high-energy laser (HEL) system designs. Basically, this means that a diffraction-limited beam must be emitted and kept on target. The purpose of the Grating Beam Combiner (GBC) Program is to develop a key element of a beam control system concept designated the Total Optical Control System (TOCS). The grating beam combiner is a compound grating designed to provide beam samples that are diffracted in the same direction, independent of angle of incidence, provided the input beams are exactly counterpropagating.

The objectives of this effort were:

- To analyze the fabrication tolerances of the GBC and their implications for system design.

- To fabricate small-scale GBC's using manufacturing processes and materials appropriate to a full-scale version to produce: (1) a GBC whose groove depths and frequencies are those of an operational design appropriate to the Large Optics Demonstration Experiment (LODE) and (2) a second GBC with depths and frequencies suitable for a laboratory boresight demonstration experiment.

- To characterize the fabricated GBC's by measuring the frequencies, groove depths, optical figure, and diffracted wavefront quality.

- To demonstrate the boresighting performance of the GBC in the laboratory, specifically showing the invariance of the co-boresighting with angle of incidence.

The feature that differentiates the TOCS concept from other beam control systems is that incoming beam sampling is combined with high-energy beam sampling in a unique manner. Figure 1-1 shows a simplified block diagram of the TOCS concept. The target is illuminated with a ultraviolet (UV) laser. The return UV energy is directed to the wavefront/tilt sensor by the grating beam combiner. The wavefront error of the transmitter optics (and atmosphere, if any) and target direction are measured and subsequently corrected by deformable/tilt mirror no. 1. The GBC also samples the high-energy beam and sends the sample to the common wavefront/tilt sensor that commands the deformable/tilt mirror no. 2 to "clean up" the high-energy beam and send it in the same direction as the incident UV beam. The net result is that a high optical quality high-energy beam is directed to the target without the requirement for accurately boresighting or mechanically referencing separate systems together.

The feasibility of the wavefront/tilt sensor and the deformable tilt mirrors has been demonstrated on other programs and their development is continuing. This contract addresses the development of the grating beam combiner portion of the overall TOCS concept.

1
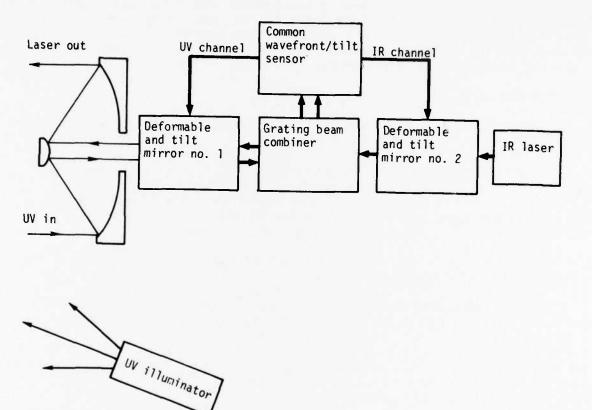
Fig. 1-1 -- Basic TOCS concept

2

2. ANALYSIS

2.1 GBC PRINCIPLE

The grating beam combiner (GBC) utilizes two grating frequencies and a retroreflector to co-boresight an infrared (IR) diffraction order with an ultraviolet (UV) diffraction order. The concept is shown schematically in Fig. 2.1.

Most of the IR energy is reflected by the GBC. A weaker non-zero diffraction order is sent to a retroreflector, from which it returns and is diffracted again. The two diffractions provide an IR sample sufficiently attenuated (by about 10^{-11}) for a wavefront sensor.

The UV beam, a return from an illuminated target, is incident antiparallel to the outgoing IR beam. It diffracts once from the GBC. Because of the extreme wavelength ratio, it is possible to diffract the weaker UV beam* with much higher efficiency (about 30%).

The grating equations that govern these diffractions are:

$$\sin \theta_{i'} + \sin \phi = m \lambda_{IR} f_1 \text{ first diffraction of IR}$$

$$\sin \phi + \sin \theta_{IR} = n \lambda_{IR} f_2 \text{ second diffraction of IR}$$

$$\sin (-\theta_i) + \sin \theta_{UV} = p \lambda_{UV} f_1 \text{ diffraction of UV}$$

The meanings of the various angles are illustrated in Fig. 2-1.

Combining the three equations so that $\sin\phi$ and $\sin\theta_i$ are eliminated yields

$$-\sin \theta_{IR} + \sin \theta_{UV} = m \lambda_{IR} f_1 - n \lambda_{IR} f_2 + p \lambda_{UV} f_1$$

---

*It is not necessary that the designator beam be UV or that the HEL beam be any particular IR wavelength. A solution can be found for any pair of wavelengths.

3
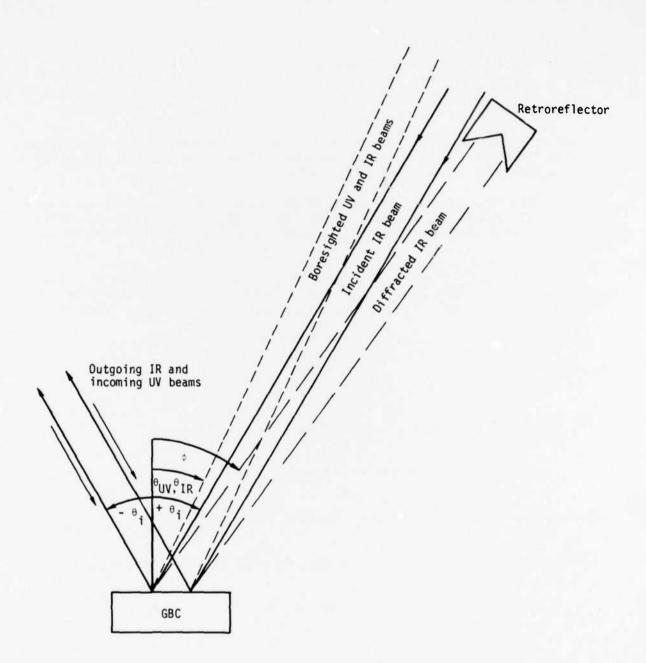
Fig. 2-1 -- Grating beam combiner concept

4

For the boresight condition, $\theta_{IR} = \theta_{UV}$ requiring

$$\frac{f_2}{f_1} = \frac{m\lambda_{IR} + p\lambda_{UV}}{n\lambda_{IR}}$$

So long as the two spatial frequencies are in this ratio the diffracted orders will be boresighted in the same direction, independent of their angle of incidence on the grating. Hence, any boresight difference measured by a sensor is related only to the off-set between the outgoing IR and the incoming UV beams.

In practice, tolerances on GBC frequency ratio and residual misalignment between frequencies generate some apparent offset even when the target is boresighted. These are analyzed in Section 2.3 and are shown to be small for achievable tolerances on these parameters.

A more general design is described in Appendix A.

2.2 GRATING EFFICIENCY

In general, the efficiency of a simple plane grating is a complicated function of groove profile, wavelength, angle of incidence, and substrate optical constants. For an infinitely conducting substrate having sinusoidal grooves whose depth is small compared to the period, at a wavelength short compared to the period, scalar theory predicts

$$\epsilon_n = J_n^2 \left(\frac{2\pi\delta}{\lambda} \right)$$

where ϵ_n = efficiency of n-th order diffraction =

   n-th order intensity/total intensity

δ = peak-to-peak sinusoidal groove depth

λ = wavelength

These conditions are satisfied with the GBC at the assumed ultraviolet wavelength ($\lambda = 0.35$ μm). At $\lambda = 2.7$ μm, the ratio λ/d is 0.54. This is a regime where scalar theory does not strictly hold, though it represents reasonable accuracy for design purposes. Actual efficiency at 2.7 μm will depend to some extent on polarization and angle of incidence.

For the operational grating, second-order is selected for the IR diffractions so that low efficiency diffraction and high reflectance of the HEL beam is achieved.

5

The scalar efficiency formulas that govern this design are

$$\epsilon_{2.7} = \left[J_0^2 \left(\frac{2\pi x_1}{2.7} \right) J_2^2 \left(\frac{2\pi x_1}{2.7} \right) \right] \left[J_0^2 \left(\frac{2\pi x_2}{2.7} \right) J_2^2 \left(\frac{2\pi x_2}{2.7} \right) \right] \equiv f(x_1) \ f(x_2)$$

$$\epsilon_{0.35} = J_1^2 \left(\frac{2\pi x_1}{0.35} \right) J_0^2 \left(\frac{2\pi x_2}{0.35} \right)$$

$$\equiv g(x_1) \ h(x_2)$$

where E_λ = efficiency at wavelength λ

x_1, x_2 = peak-to-peak groove depth

The efficiency factors f, g, and h are plotted in Figs. 2-2 and 2-3. From the above formulas and the curves, the design values (Section 2.5) for grating groove depth can be understood in terms of their effect on efficiency at the two wavelengths and tolerances thereon. Groove depth x_1 is chosen for maximum first-order diffraction efficiency at 0.35 μm. Groove depth x_2 is chosen so that, in conjunction with the chosen value of x_1, a low diffraction efficiency (1.4×10^{-11}) for the IR sample beam is achieved.

A computation of the direction and efficiency of IR and UV orders (up to 10th order) diffracted by the operational GBC is summarized in Tables 2-1, 2-2, and 2-3. Approximately 3% of the energy is diffracted out of the HEL beam. This energy must be absorbed or dumped out of the system.

2.3 BORESIGHT ERRORS BETWEEN WAVEFRONT SENSOR BEAMS--FIRST-ORDER FORMULAS

There are several causes of boresight differences between the UV and IR wavefront sensor beams. Fabricated to perfection, with precisely counter-propagating beams illuminating it, the GBC will, as has been shown, produce sample beams that are exactly co-aligned. If either the spatial frequency ratio or the alignment between spatial frequencies departs from the design values, offsets will be introduced. Departures from antiparallelism between the incoming UV and outgoing IR also produce boresight differences that the wavefront sensor is designed to measure.

6

1.00
(×10⁻⁴)

0.80

Depth x_1

Efficiency Factor

0.60

0.40

$$J_0^2 \left(\frac{2\pi x}{\lambda_{IR}}\right) J_2^2 \left(\frac{2\pi x}{\lambda_{IR}}\right) = f(x)$$

$\lambda_{IR} = 2.7$ μm

0.20

Depth x_2

0

0   0.050   0.100   0.150

Peak-to-Peak Groove Depth, μm
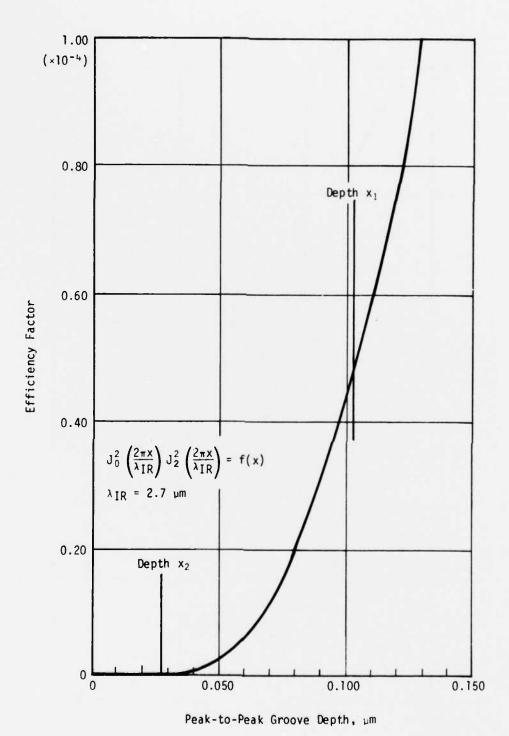
Fig. 2-2 -- Efficiency factor versus groove depth -- $\lambda = 2.7$ μm

7
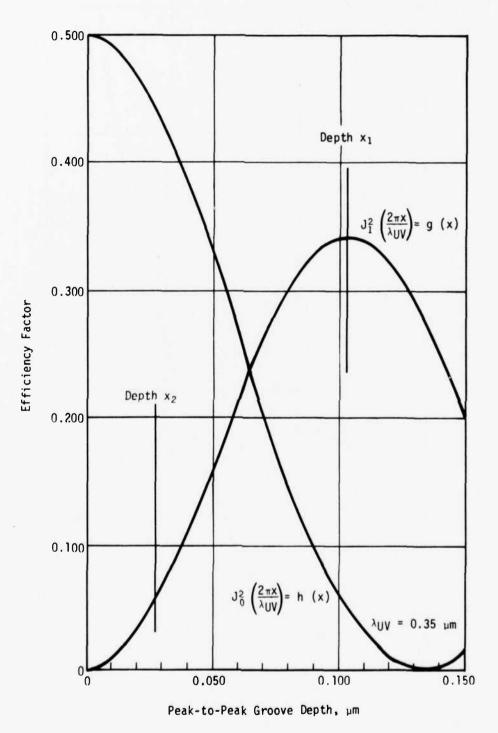
Fig. 2.3 -- Efficiency factor versus groove depth -- $\lambda = 0.35 \ \mu m$

Table 2-1 -- Intensities and Directions of Orders Diffracted
by the GBC From the Incident HEL Beam
($\theta_i = 60°$, Incident Intensity = 1)

SORTED BY ANGLE:

ANGLE	INTENSITY	ORDERS
-76.174	0.256E-17	(-3, 3)
-69.394	0.138E-10	(-2, 2)
-64.293	0.147E-04	(-1, 1)
-60.000	0.970E+00	(0, 0)
-56.204	0.147E-04	(1, -1)
-52.752	0.138E-10	(2, -2)
-49.555	0.256E-17	(3, -3)
-46.554	0.150E-24	(4, -4)
-43.711	0.358E-32	(5, -5)
-42.534	0.0	(5, -5)
-40.997	0.414E-40	(-6, 6)
-39.868	0.123E-61	(-8, 9)
-38.391	0.258E-48	(7, -7)
-37.303	0.428E-53	(-7, 8)
-35.875	0.941E-57	(8, -8)
-34.822	0.896E-45	(-6, 7)
-33.437	0.215E-65	(9, -9)
-32.413	0.106E-36	(-5, 6)
-31.066	0.0	(-5, 6)
-30.068	0.636E-29	(-4, 5)
-27.777	0.170E-21	(-3, 4)
-25.533	0.163E-14	(-2, 3)
-23.330	0.391E-08	(-1, 2)
-21.163	0.103E-02	(0, 1)
-19.028	0.139E-01	(1, 0)
-16.919	0.521E-07	(2, -1)
-14.834	0.217E-13	(3, -2)
-12.764	0.226E-20	(4, -3)
-10.721	0.844E-28	(5, -4)
-8.686	0.140E-35	(6, -5)
-7.818	0.0	(6, -5)
-6.663	0.119E-43	(7, -6)
-5.798	0.560E-58	(-7, 9)
-4.648	0.568E-52	(8, -7)
-3.786	0.149E-49	(-6, 8)
-2.638	0.164E-60	(9, -8)
-1.778	0.229E-41	(-5, 7)
-0.632	0.0	(-5, 7)
0.228	0.187E-33	(-4, 6)
2.234	0.721E-26	(-3, 5)
4.242	0.108E-18	(-2, 4)
6.256	0.461E-12	(-1, 3)
8.278	0.274E-06	(0, 2)
10.310	0.147E-04	(1, 1)
12.355	0.490E-04	(2, 0)
14.417	0.817E-10	(3, -1)
16.497	0.191E-16	(4, -2)
18.601	0.137E-23	(5, -3)
20.730	0.331E-31	(6, -4)
22.891	0.404E-39	(7, -5)
23.827	0.595E-63	(-7, 10)
25.086	0.262E-47	(8, -6)
26.038	0.195E-54	(-6, 9)
27.321	0.987E-56	(9, -7)
28.292	0.380E-46	(-5, 8)
29.602	0.231E-64	(10, -8)
30.595	0.406E-38	(-4, 7)
32.954	0.213E-30	(-3, 6)
35.378	0.460E-23	(-2, 5)
37.877	0.306E-16	(-1, 4)
40.464	0.323E-10	(0, 3)
43.155	0.391E-08	(1, 2)
45.970	0.521E-07	(2, 1)
48.936	0.769E-07	(3, 0)
52.089	0.721E-13	(4, -1)
55.484	0.108E-19	(5, -2)
59.201	0.498E-27	(6, -3)
63.377	0.951E-35	(7, -4)
68.275	0.889E-43	(8, -5)
70.729	0.207E-59	(-6, 10)
74.573	0.456E-51	(9, -6)
78.229	0.498E-51	(-5, 9)
87.400	0.139E-59	(10, -7)

Table 2-2 -- Intensities and Directions of Orders Diffracted
by the GBC From the Retroreflector Return

```
SORTED BY ANGLE:
ANGLE          INTENSITY        ORDERS

-87.402        0.270E-56      ( -8,   7)
-78.229        0.275E-62      (  7,  -9)
-74.573        0.584E-48      ( -7,   6)
-70.729        0.0            ( -7,   6)
-68.275        0.688E-40      ( -6,   5)
-63.377        0.414E-32      ( -5,   4)
-59.201        0.111E-24      ( -4,   3)
-55.484        0.106E-17      ( -3,   2)
-52.089        0.255E-11      ( -2,   1)
-48.936        0.680E-06      ( -1,   0)
-45.970        0.505E-07      (  0,  -1)
-43.155        0.192E-12      (  1,  -2)
-40.464        0.800E-19      (  2,  -3)
-37.877        0.833E-26      (  3,  -4)
-35.378        0.312E-33      (  4,  -5)
-34.331        0.0            (  4,  -5)
-32.954        0.518E-41      (  5,  -6)
-31.936        0.0            (  5,  -6)
-30.595        0.440E-49      (  6,  -7)
-29.602        0.462E-61      ( -8,   8)
-28.292        0.210E-57      (  7,  -8)
-27.321        0.126E-52      ( -7,   7)
-26.038        0.0            ( -7,   7)
-25.086        0.203E-44      ( -6,   6)
-23.827        0.0            ( -6,   6)
-22.891        0.176E-36      ( -5,   5)
-20.730        0.734E-29      ( -4,   4)
-18.601        0.125E-21      ( -3,   3)
-16.497        0.678E-15      ( -2,   2)
-14.417        0.722E-09      ( -1,   1)
-12.355        0.476E-04      (  0,   0)
-10.310        0.722E-09      (  1,  -1)
 -8.278        0.678E-15      (  2,  -2)
 -6.256        0.125E-21      (  3,  -3)
 -4.242        0.734E-29      (  4,  -4)
 -2.234        0.176E-36      (  5,  -5)
 -1.374        0.0            (  5,  -5)
 -0.228        0.203E-44      (  6,  -6)
  0.632        0.0            (  6,  -6)
  1.778        0.126E-52      (  7,  -7)
  2.638        0.210E-57      ( -7,   8)
  3.786        0.462E-61      (  8,  -8)
  4.648        0.440E-49      ( -6,   7)
  5.798        0.0            ( -6,   7)
  6.663        0.518E-41      ( -5,   6)
  7.818        0.0            ( -5,   6)
  8.686        0.312E-33      ( -4,   5)
 10.721        0.833E-26      ( -3,   4)
 12.769        0.800E-19      ( -2,   3)
 14.834        0.192E-12      ( -1,   2)
 16.919        0.505E-07      (  0,   1)
 19.028        0.680E-06      (  1,   0)
 21.163        0.255E-11      (  2,  -1)
 23.330        0.106E-17      (  3,  -2)
 25.533        0.111E-24      (  4,  -3)
 27.777        0.414E-32      (  5,  -4)
 30.068        0.688E-40      (  6,  -5)
 31.066        0.0            (  6,  -5)
 32.413        0.584E-48      (  7,  -6)
 33.437        0.275E-62      ( -7,   9)
 34.822        0.278E-56      (  8,  -7)
 35.875        0.729E-54      ( -6,   8)
 37.303        0.803E-65      (  9,  -8)
 38.391        0.112E-45      ( -5,   7)
 39.868        0.0            ( -5,   7)
 40.997        0.919E-38      ( -4,   6)
 43.711        0.353E-30      ( -3,   5)
 46.554        0.531E-23      ( -2,   4)
 49.555        0.226E-16      ( -1,   3)
 52.752        0.134E-10      (  0,   2)
 56.204        0.722E-09      (  1,   1)
 60.000        0.240E-08      (  2,   0)
 64.293        0.401E-14      (  3,  -1)
 69.394        0.938E-21      (  4,  -2)
 76.174        0.624E-29      (  5,  -3)
```

10

SORTED BY ANGLE:

ANGLE	INTENSITY	ORDERS
-29.249	0.847E-39	(-10,-10)
-25.033	0.134E-35	(-10, -9)
-24.746	0.995E-37	(-9,-10)
-20.958	0.172E-32	(-10, -8)
-20.679	0.157E-33	(-9, -9)
-20.402	0.944E-35	(-8,-10)
-16.991	0.174E-28	(-10, -7)
-16.719	0.202E-30	(-9, -8)
-16.448	0.149E-31	(-8, -9)
-16.177	0.704E-33	(-7,-10)
-13.106	0.134E-26	(-10, -6)
-12.839	0.204E-27	(-9, -7)
-12.573	0.191E-28	(-8, -8)
-12.306	0.111E-29	(-7, -9)
-12.040	0.399E-31	(-6,-10)
-9.282	0.763E-24	(-10, -5)
-9.018	0.158E-24	(-9, -6)
-8.755	0.193E-25	(-8, -7)
-8.492	0.143E-26	(-7, -8)
-8.230	0.631E-28	(-6, -9)
-7.967	0.165E-29	(-5,-10)
-5.499	0.301E-21	(-10, -4)
-5.238	0.897E-22	(-9, -5)
-4.977	0.150E-22	(-8, -6)
-4.716	0.144E-23	(-7, -7)
-4.455	0.808E-25	(-6, -8)
-4.194	0.260E-26	(-5, -9)
-3.934	0.463E-28	(-4,-10)
-1.740	0.757E-19	(-10, -3)
-1.480	0.353E-19	(-9, -4)
-1.220	0.850E-20	(-8, -5)
-0.960	0.112E-20	(-7, -6)
-0.700	0.817E-22	(-6, -7)
-0.440	0.333E-23	(-5, -8)
-0.180	0.732E-25	(-4, -9)
0.080	0.809E-27	(-3,-10)
2.012	0.107E-16	(-10, -2)
2.272	0.889E-17	(-9, -3)
2.532	0.335E-17	(-8, -4)
2.792	0.634E-18	(-7, -5)
3.052	0.633E-19	(-6, -6)
3.313	0.337E-20	(-5, -7)
3.573	0.938E-22	(-4, -8)
3.834	0.128E-23	(-3, -9)
4.094	0.747E-26	(-2,-10)
5.772	0.662E-15	(-10, -1)
6.033	0.125E-14	(-9, -2)
6.294	0.843E-15	(-8, -3)
6.556	0.250E-15	(-7, -4)
6.818	0.359E-16	(-6, -5)
7.080	0.261E-17	(-5, -6)
7.342	0.946E-19	(-4, -7)
7.604	0.164E-20	(-3, -8)
7.866	0.118E-22	(-2, -9)
8.129	0.257E-25	(-1,-10)
9.557	0.982E-14	(-10, 0)
9.821	0.777E-13	(-9, -1)
10.084	0.119E-12	(-8, -2)
10.349	0.623E-13	(-7, -3)
10.613	0.142E-13	(-6, -4)
10.878	0.148E-14	(-5, -5)

11.142	C.734E-
11.407	C.166E-
11.673	C.151E-
11.938	C.405E-
12.204	0.787E-
13.385	C.662E-
13.652	C.115E-
13.920	C.737E-
14.188	C.887E-
14.456	C.357E-
14.725	0.584E-
14.994	C.417E-
15.263	C.128E-
15.533	C.153E-
15.802	C.520E-
16.073	C.124E-
16.344	C.257E-
17.275	C.107E-
17.547	C.777E-
17.820	C.109E-0
18.093	C.550E-0
18.367	C.503E-0
18.641	C.147E-
18.916	C.164E-
19.191	C.729E-1
19.466	C.118E-
19.742	C.526E-
20.018	C.159E-1
20.295	C.406E-2
20.573	C.747E-2
21.249	C.757E-
21.528	C.125E-
21.807	C.737E-
22.088	C.815E-0
22.369	C.312E-0
22.650	C.207E-0
22.932	C.414E-0
23.214	C.287E-09
23.499	C.673E-1
23.781	C.407E-1
24.066	C.161E-1
24.351	C.520E-1
24.636	C.118E-2
24.923	C.809E-2
25.333	C.301E-2
25.621	C.869E-1
25.910	C.119E-1
26.199	C.550E-09
26.489	C.462E-06
26.780	C.126E-0
27.071	C.563E-0
27.364	C.723E-07
27.657	C.265E-08
27.951	C.231E-10
28.245	C.125E-13
28.541	C.526E-16
28.837	C.151E-19
29.134	C.128E-23
29.432	C.443E-2
29.560	C.763E-19
29.860	C.353E-19
30.160	0.843E-1
30.461	C.887E-1
30.763	C.312E-07
31.066	C.191E-04
31.370	C.362E-04
31.675	C.102E-0
31.981	C.667E-06

Table 2-3 -- Intensities and Directions of Orders Diffracted by the GBC From the UV Beam ($\theta_i = 60°$, Incident Intensity = 1)

11.142	0.734E-16	(-4, -6)	32.288	0.912E-08	(-1, -4)
11.407	0.166E-17	(-3, -7)	32.596	0.706E-11	(0, -5)
11.673	0.151E-18	(-2, -8)	32.905	0.407E-15	(1, -6)
11.938	0.405E-22	(-1, -9)	33.215	0.153E-16	(2, -7)
12.204	0.787E-26	(0, -10)	33.526	0.164E-25	(3, -8)
13.385	0.666E-15	(-10, 1)	33.839	0.732E-25	(4, -9)
13.652	0.115E-11	(-9, 0)	33.973	0.134E-26	(-10, 6)
13.920	0.737E-11	(-8, -1)	34.152	0.165E-29	(5, -10)
14.188	0.887E-11	(-7, -2)	34.287	0.897E-22	(-9, 5)
14.456	0.357E-11	(-6, -3)	34.602	0.335E-17	(-8, 4)
14.725	0.584E-12	(-5, -4)	34.919	0.629E-13	(-7, 3)
14.994	0.417E-13	(-4, -5)	35.236	0.503E-09	(-6, 2)
15.263	0.128E-14	(-3, -6)	35.555	0.129E-05	(-5, 1)
15.533	0.153E-16	(-2, -7)	35.875	0.536E-03	(-4, 0)
15.802	0.520E-19	(-1, -8)	36.197	0.632E-03	(-3, -1)
16.073	0.124E-22	(0, -9)	36.520	0.941E-04	(-2, -2)
16.344	0.257E-25	(1, -10)	36.844	0.230E-05	(-1, -3)
17.275	0.107E-16	(-10, 2)	37.169	0.279E-08	(0, -4)
17.547	0.777E-12	(-9, 1)	37.496	0.231E-11	(1, -5)
17.820	0.109E-09	(-8, 0)	37.825	0.116E-13	(2, -6)
18.093	0.550E-09	(-7, -1)	38.154	0.166E-17	(3, -7)
18.367	0.503E-09	(-6, -2)	38.486	0.936E-22	(-4, -8)
18.641	0.147E-09	(-5, -3)	38.628	0.174E-26	(-10, 7)
18.916	0.164E-10	(-4, -4)	38.819	0.260E-26	(5, -9)
19.191	0.729E-12	(-3, -5)	38.962	0.158E-24	(-9, 6)
19.466	0.118E-13	(-2, -6)	39.153	0.399E-31	(6, -10)
19.742	0.526E-16	(-1, -7)	39.297	0.850E-20	(-8, 5)
20.018	0.159E-19	(0, -8)	39.634	0.250E-15	(-7, 4)
20.295	0.406E-22	(1, -9)	39.972	0.357E-11	(-6, 3)
20.573	0.747E-26	(2, -10)	40.312	0.207E-07	(-5, 2)
21.249	0.757E-16	(-10, 3)	40.654	0.362E-04	(-4, 1)
21.528	0.125E-14	(-9, 2)	40.997	0.938E-02	(-3, 0)
21.807	0.737E-11	(-8, 1)	41.343	0.583E-02	(-2, -1)
22.088	0.815E-08	(-7, 0)	41.690	0.324E-03	(-1, -2)
22.369	0.312E-07	(-6, -1)	42.039	0.703E-06	(0, -3)
22.650	0.207E-07	(-5, -2)	42.390	0.912E-08	(1, -4)
22.932	0.414E-08	(-4, -3)	42.743	0.673E-11	(2, -5)
23.214	0.287E-09	(-3, -4)	43.098	0.128E-14	(3, -6)
23.494	0.673E-11	(-2, -5)	43.455	0.944E-19	(4, -7)
23.781	0.407E-13	(-1, -6)	43.609	0.172E-32	(-10, 8)
24.066	0.161E-16	(0, -7)	43.814	0.333E-23	(5, -8)
24.351	0.520E-19	(1, -8)	43.969	0.204E-27	(-9, 7)
24.636	0.118E-22	(2, -9)	44.175	0.631E-28	(6, -9)
24.923	0.809E-27	(3, -10)	44.331	0.150E-22	(-8, 6)
25.333	0.301E-21	(-10, 4)	44.539	0.704E-33	(7, -10)
25.621	0.869E-17	(-9, 3)	44.696	0.634E-15	(-7, 5)
25.910	0.119E-12	(-8, 2)	45.062	0.142E-13	(-5, 4)
26.199	0.556E-09	(-7, 1)	45.432	0.147E-09	(-5, 3)
26.489	0.462E-06	(-6, 0)	45.803	0.583E-06	(-4, 2)
26.780	0.126E-05	(-5, -1)	46.177	0.632E-03	(-3, 1)
27.071	0.583E-06	(-4, -2)	46.554	0.865E-01	(-2, 0)
27.364	0.723E-07	(-3, -3)	46.934	0.201E-01	(-1, -1)
27.657	0.265E-08	(-2, -4)	47.316	0.991E-04	(0, -2)
27.951	0.231E-10	(-1, -5)	47.700	0.230E-05	(1, -3)
28.245	0.125E-13	(0, -6)	48.088	0.265E-08	(2, -4)
28.541	0.526E-16	(1, -7)	48.479	0.729E-12	(3, -5)
28.837	0.151E-19	(2, -8)	48.872	0.734E-16	(4, -6)
29.134	0.128E-22	(3, -9)	49.042	0.134E-35	(-10, 9)
29.432	0.463E-27	(4, -10)	49.269	0.337E-20	(5, -7)
29.560	0.763E-24	(-10, 5)	49.440	0.202E-30	(-9, 8)
29.860	0.353E-19	(-9, 4)	49.669	0.806E-25	(6, -8)
30.160	0.843E-15	(-8, 3)	49.842	0.193E-25	(-8, 7)
30.461	0.887E-11	(-7, 2)	50.073	0.111E-29	(7, -9)
30.763	0.312E-07	(-6, 1)	50.246	0.112E-20	(-7, 6)
31.066	0.191E-04	(-5, 0)	50.479	0.944E-35	(8, -10)
31.370	0.303E-04	(-4, -1)	50.655	0.359E-16	(-6, 5)
31.675	0.103E-04	(-3, -2)	51.067	0.584E-12	(-5, 4)
31.981	0.667E-06	(-2, -3)	51.482	0.414E-08	(-4, 3)

Angle	Intensity	Order		Angle	Intensity	Order
32.288	0.912E-08	(-1, -4)		51.901	0.102E-04	(-3, 2)
32.596	0.708E-11	(0, -5)		52.325	0.583E-02	(-2, 1)
32.905	0.407E-13	(1, -6)		52.752	0.298E+00	(-1, 0)
33.215	0.153E-16	(2, -7)		53.164	0.614E-02	(0, -1)
33.526	0.164E-20	(3, -8)		53.620	0.324E-03	(1, -2)
33.839	0.732E-25	(4, -9)		54.060	0.667E-06	(2, -3)
33.973	0.134E-28	(-10, 6)		54.506	0.287E-09	(3, -4)
34.152	0.165E-29	(5, -10)		54.956	0.417E-13	(4, -5)
34.287	0.897E-22	(-9, 5)		55.150	0.847E-39	(-10, 10)
34.602	0.335E-17	(-8, 4)		55.411	0.261E-17	(5, -6)
34.919	0.629E-13	(-7, 3)		55.608	0.157E-33	(-9, 9)
35.236	0.503E-09	(-6, 2)		55.872	0.617E-22	(6, -7)
35.555	0.129E-05	(-5, 1)		56.071	0.191E-28	(-8, 8)
35.875	0.536E-03	(-4, 0)		56.338	0.143E-26	(7, -8)
36.197	0.632E-03	(-3, -1)		56.539	0.144E-23	(-7, 7)
36.520	0.941E-04	(-2, -2)		56.810	0.149E-31	(8, -9)
36.844	0.230E-05	(-1, -3)		57.014	0.633E-19	(-6, 6)
37.169	0.279E-08	(0, -4)		57.288	0.995E-37	(9, -10)
37.496	0.231E-10	(1, -5)		57.494	0.148E-14	(-5, 5)
37.825	0.118E-13	(2, -6)		57.981	0.164E-10	(-4, 4)
38.154	0.166E-17	(3, -7)		58.475	0.723E-07	(-3, 3)
38.486	0.938E-22	(4, -8)		58.976	0.941E-04	(-2, 2)
38.628	0.174E-29	(-10, 7)		59.484	0.201E-01	(-1, 1)
38.819	0.260E-26	(5, -9)		60.000	0.911E-01	(0, 0)
38.962	0.158E-24	(-9, 6)		60.524	0.201E-01	(1, -1)
39.153	0.399E-31	(6, -10)		61.057	0.941E-04	(2, -2)
39.297	0.850E-20	(-8, 5)		61.598	0.723E-07	(3, -3)
39.634	0.250E-15	(-7, 4)		62.150	0.164E-10	(4, -4)
39.972	0.357E-11	(-6, 3)		62.711	0.148E-14	(5, -5)
40.312	0.207E-07	(-5, 2)		62.956	0.995E-37	(-9, 10)
40.654	0.362E-04	(-4, 1)		63.284	0.633E-19	(6, -6)
40.997	0.938E-02	(-3, 0)		63.533	0.149E-31	(-8, 9)
41.343	0.583E-02	(-2, -1)		63.868	0.144E-23	(7, -7)
41.690	0.324E-03	(-1, -2)		64.122	0.143E-26	(-7, 8)
42.039	0.703E-06	(0, -3)		64.465	0.191E-28	(8, -8)
42.390	0.912E-08	(1, -4)		64.725	0.817E-22	(-6, 7)
42.743	0.673E-11	(2, -5)		65.075	0.157E-33	(9, -9)
43.098	0.128E-14	(3, -6)		65.340	0.261E-17	(-5, 6)
43.455	0.948E-19	(4, -7)		65.699	0.847E-39	(10, -10)
43.609	0.172E-32	(-10, 8)		65.971	0.417E-13	(-4, 5)
43.814	0.333E-23	(5, -8)		66.618	0.287E-09	(-3, 4)
43.969	0.204E-27	(-9, 7)		67.282	0.667E-06	(-2, 3)
44.175	0.631E-28	(6, -9)		67.964	0.324E-03	(-1, 2)
44.331	0.150E-22	(-8, 6)		68.668	0.614E-02	(0, 1)
44.539	0.704E-33	(7, -10)		69.394	0.298E+00	(1, 0)
44.696	0.634E-18	(-7, 5)		70.146	0.583E-02	(2, -1)
45.062	0.142E-13	(-6, 4)		70.926	0.102E-04	(3, -2)
45.432	0.947E-09	(-5, 3)		71.738	0.414E-08	(4, -3)
45.803	0.583E-04	(-4, 2)		72.587	0.584E-12	(5, -4)
46.177	0.632E-03	(-3, 1)		73.478	0.359E-16	(6, -5)
46.554	0.865E-01	(-2, 0)		73.874	0.944E-38	(-8, 10)
46.934	0.201E-01	(-1, -1)		74.418	0.112E-20	(7, -6)
47.316	0.991E-04	(0, -2)		74.838	0.111E-29	(-7, 9)
47.700	0.230E-05	(1, -3)		75.417	0.193E-25	(8, -7)
48.088	0.265E-08	(2, -4)		75.866	0.808E-25	(-6, 8)
48.479	0.729E-12	(3, -5)		76.488	0.202E-30	(9, -8)
48.872	0.734E-16	(4, -6)		76.974	0.337E-26	(-5, 7)
49.042	0.134E-35	(-10, 9)		77.650	0.134E-35	(10, -9)
49.269	0.337E-26	(5, -7)		78.182	0.734E-16	(-4, 6)
49.440	0.202E-30	(-9, 8)		79.527	0.729E-12	(-3, 5)
49.669	0.808E-25	(6, -8)		81.069	0.265E-08	(-2, 4)
49.842	0.193E-25	(-8, 7)		82.938	0.230E-05	(-1, 3)
50.073	0.111E-29	(7, -9)		85.525	0.991E-04	(0, 2)
50.246	0.112E-20	(-7, 6)				
50.479	0.944E-35	(8, -10)				
50.655	0.359E-16	(-6, 5)				
51.067	0.584E-12	(-5, 4)				
51.482	0.414E-08	(-4, 3)				

As shown in Appendix B, the boresight error due to a grating spatial frequency ratio error is:

$$\Delta\theta_{UV-IR} = \left(\frac{f_1 n \lambda_{IR}}{\cos\theta_{IR}}\right)\delta\left(\frac{f_2}{f_1}\right)$$

where: f_1 = grating frequency no. 1
      n = IR order diffracted into wavefront sensor
      λ_{IR} = IR wavelength
      θ_{IR} = angle of diffraction of IR order
    $\Delta\theta_{UV-IR}$ = azimuthal boresight error
    $\delta(f_2/f_1)$ = design spatial frequency ratio-actual ratio

The error due to a skew, ϵ, between grating frequencies (i.e., angular misalignment in the grating plane) is simply

$$\Delta\phi = \epsilon$$

$\Delta\phi$ is an elevation error and adds in quadrature to azimuthal errors.

The boresight errors seen by the wavefront sensor due to input beam misalignment are

$$\Delta\theta_{UV-IR} = \left(\frac{\cos i}{\cos\theta_{IR}}\right)\Delta\theta_i$$

$$\Delta\phi_{UV-IR} = \Delta\phi_i$$

2.4 BORESIGHT ERRORS BETWEEN WAVEFRONT SENSOR BEAMS--NUMERICAL CALCULATIONS

To check the first-order analyses in Section 2.3, an exact numerical calculation of the boresight errors was performed. The code treats each incident, intermediate, and final beam as a ray (3-D vector). Following the initial diffraction of the IR beam and its return by the retroreflector, the inter-grating skew is introduced as an exact rotation. The actual frequency ratio is also introduced exactly.

The simulation has been carried out for a grid of skews and frequency ratio residuals. For each case, the UV-IR beam skew (both x and y components) were calculated: (1) versus angle of incidence and (2) versus input boresight error.

Typical results of this simulation for an operational GBC are given in Figs. 2-4 and 2-5. In both figures, the y-axis is the overall magnitude of the skew. As predicted, output beam skew depends linearly on input beam skew, with an offset if there is a frequency ratio residual. The input boresight offset was specified to be purely azimuthal, so the compound effect when frequency ratio residual is nonzero is still a purely azimuthal output skew.

13
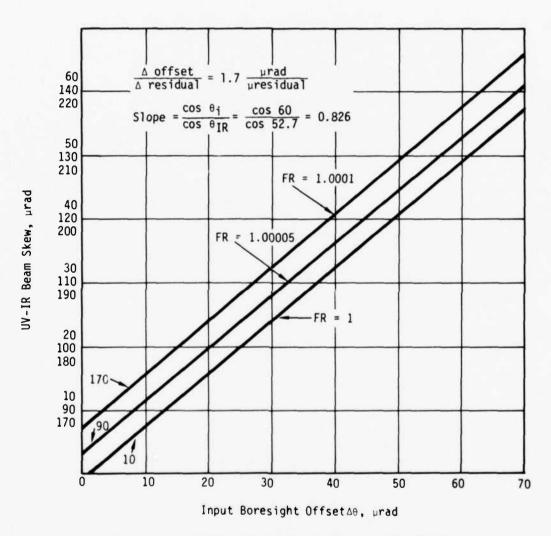
Fig. 2-4 -- Beam skew versus input boresight offset
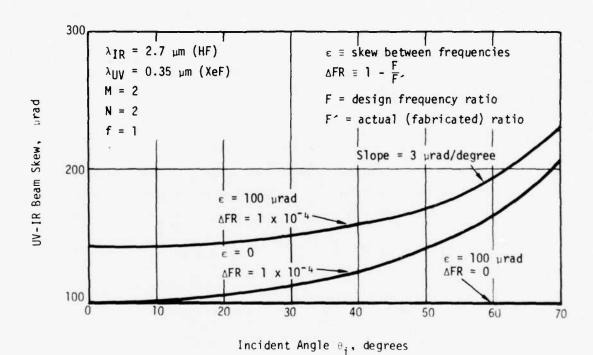
Fig. 2-5 -- Beam skew versus incidence angle

The boresight invariance of the GBC is impacted slightly by a frequency ratio residual. This is shown in Fig. 2-5 to be 3 μrad/degree at an angle of incidence of 60°, a small effect relative to the offset. The uppermost of these curves results from the addition in quadrature of nonzero vertical and horizontal components of output error. By itself, inter-grating skew does not affect the boresight invariance at all.

2.5 DESIGN PARAMETER SUMMARY

Two versions of the grating beam combiner were designed and fabricated: (1) an operational grating with frequencies and groove depths appropriate to LODE, and (2) a high-efficiency design for use in a laboratory boresight demonstration using helium-neon wavelengths (0.6328 and 3.39 μm). The design parameters for these gratings are summarized in Table 2-4.

The performance of the grating beam combiner will depend on how closely it approaches its design specifications. Accordingly, a set of tolerances applicable to the GBC were established and are summarized in Table 2-5. These represented a composite goal for components fabricated on this program.

Table 2-4 -- Design Specifications

	Operational Grating	Boresight Demonstration Grating
m, n, p	$\pm 2, \pm 2, \mp 1$	$\pm 1, \pm 1, \pm 1$
λ_{IR}	2.7 μm	3.39 μm
λ_{UV}	0.35 μm	0.6328 μm
f_2/f_1	0.9352	1.1866
x_1	0.10 μm	0.1 μm
x_2	0.028 μm	0.1 μm
f_1	$(5.00 \text{ μm})^{-1}$	$(5.933 \text{ μm})^{-1}$
f_2	$(5.346 \text{ μm})^{-1}$	$(5.00 \text{ μm})^{-1}$
Efficiencies		
e_{IR}	1.4×10^{-11}	
e_{UV}	0.30	

Table 2-5 -- Design Tolerances--Operational Grating

Frequency ratio residual	1.0×10^{-4}

$$\Delta FR \equiv 1 - \left(\frac{\text{actual ratio}}{\text{design ratio}}\right)$$

Boresight error due to ΔFR	2.0×10^{-4} rad

$$\Delta \theta = \left(\frac{f_1 n \lambda_{IR}}{\cos \theta_{IR}}\right) \Delta FR$$

Skew between frequencies	1.5×10^{-4} rad
Surface figure (rms)	0.025 μm
Groove figure (rms)	0.02λ
Diffracted wavefront quality	1.5×10^{-4} rad
IR sample beam (rms)	$0.07 \lambda_{IR}$
UV sample beam)rms)	$0.15 \lambda_{UV}$
Diffraction efficiency uniformity	$\dfrac{E_{min}}{E_{max}}$
IR sample beam	40%
UV sample beam	90%

3. GRATING FABRICATION

3.1 SEQUENCE OF PROCESSES

The fabrication of the final GBC consisted of five process steps: (1) substrate manufacture, (2)photoresist coating, (3) exposure, (4) development, and (5) ion milling. Each step was accompanied by process control measurement to quantify its performance. The following sections describe the development of each process step. All process steps are readily scalable to sizes required on operational high-energy lasers.
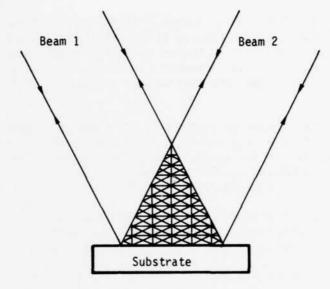
Early in the program a contact printing process was attempted. Instead of direct exposure of the photoresist in the interferometer, a grating transparency was made on high-resolution plates and contact-printed onto the photoresist. If successful this process would have eliminated the need for an ultrastable interferometer since the photographic exposure is approximately 3 seconds versus direct photoresist exposure times of as much as 1 hour. Unfortunately, the grain of the photographic emulsion generated a relief pattern in the photoresist, causing the grating to scatter a lot of energy. Thus, direct photoresist exposure in the interferometer was selected as an alternative approach.

3.2 SUBSTRATE MANUFACTURE
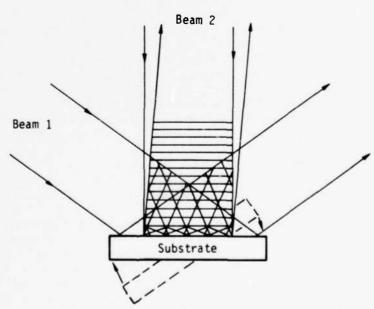
The substrates used on this program are electroless nickel-coated aluminum.* The nickel is a 125-μm-thick electroless coating into which the grating relief is transferred by ion milling to form the final grating. The nickel was polished to λ/10 over a 3-in. circular region. Substrates are rectangular, 3 by 4 by 3/4 in. thick.

Because the exposure process selected uses coherent illumination, reflections from the metal substrate can interfere to generate standing waves (see Fig. 3-1). To prevent this, an antireflection coating designed for use under photoresist is applied to the nickel. An analysis of the standing wave pattern and the details of the coating design are given in Appendices C and D.

---

*This was chosen as being representative of a cooled mirror substrate. The process used is applicable to virtually any material that can be optically polished.

(a) Exposure no. 1

(b) Exposure no. 2 [rotated as indicated
from orientation in (a)]

Fig. 3-1 -- Standing wave patterns for both GBC exposure geometries

19

3.3 PHOTORESIST COATING

The coating of the antireflection-coated substrates with photoresist is a difficult step and two different approaches have been explored. The goal was to achieve an optically flat coating of uniform thickness.

Dip coating was selected initially because it is scalable to large substrates. The rectangular shape had been specified because it is most compatible with dipping. The dip-coater was Itek-built, consisting of a slow motion pulley mechanism over a photoresist reservoir. The mechanism is enclosed to ensure a uniform draft-free environment and is capable of pulling the heavy substrates used on this program at a selectable uniform draw rate.

The photoresist coating operation begins with the thorough cleaning and baking (1 hr, 200°C) of the substrate to eliminate impurities and to drive off all solvents. After cooling to ambient temperature, the sample is suspended in the coater and lowered into the reservoir. After reaching thermal equilibrium with the photoresist bath, the pulley mechanism is started and remains activated until the substrate is clear of the bath surface.

The thickness of the resulting coating varies with the draw rate and dilution of the photoresist bath. Thicknesses from 0.2 to 1.8 μm have been achieved with dilutions in the range of 1/3 to 1/5 (parts photoresist/parts solvent) at a draw rate of 8 mm/min.
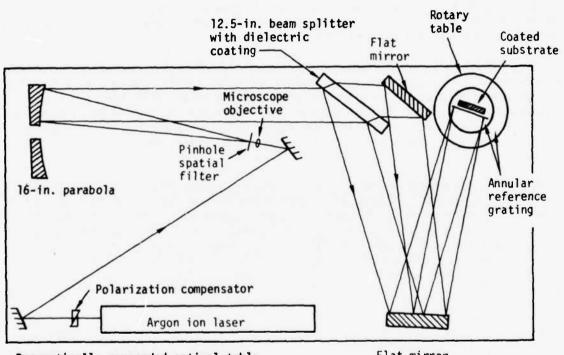
Dip coating produces acceptable uniform coatings only when the draw cycle is uninterrupted by vibrations or a fluctuation in pull rate. This was not generally found to be the case over a large number of trials. The yield was very low.

As an alternative to further experimentation with the dip coating process, a modification of the spin coating technique was tried. Since the substrates are massive relative to semiconductor wafers, it was not possible to achieve the higher angular accelerations that are generally required. By working with a lower photoresist dilution, it is possible to achieve a uniform coating even at lower speeds before the film has begun to dry. Extreme care is still required, for if drying proceeds slowly enough that radial flow is not stopped, a "stringing" relief pattern is produced. Illustrations of coating imperfections that occur with both dip and spin coating are given in Section 4.6. This technique, which we call "whirl" coating, produced excellent quality coated sub-strates with a good yield.

3.4 EXPOSURE

3.4.1 Process Interferometer

The grating exposure process must satisfy those requirements generally associated with holographic recording. These include high optical quality, total absence of stray coherent light, and good fringe visibility. The interferometer setup is shown in Fig. 3-2. The argon laser source is expanded using a microscope objective and spatial filter and collimated with an off-axis section of a 16-in. paraboloid. The expanded beam is split using a dielectrically coated 12.5-in. glass beam splitter at Brewster's angle (to eliminate a secondary reflection from the back surface). A compensator in the unexpanded beam rotates

Fig. 3-2 -- Process interferometer

its polarization to the s state. Because the angle between the interfering beams is only 5°, the impact on fringe visibility is negligible (at 90°, no fringes would be formed; see Appendix E).

The spatial uniformity of the interfering beams is limited by what can be done using conventional optics and spatial filters. The Gaussian shape of the raw beam can not be completely flattened in this way and there is a sharp trade-off between average intensity and uniformity. Uniformity as good as 10% over a 2.5-in. diameter has been achieved during many of the exposures made on this program.

The high spatial frequency grating exposure is made with the substrate normal bisecting the two interfering beams. The low spatial frequency grating is exposed with the rotary table turned to the appropriate angle.

The very long photoresist exposures require extreme mechanical and optical stability. With no control during exposure, approximately 1/2 wave stability was achieved during a 1 hour exposure after significant effort to stabilize the setup. This error was a slow drift, presumably due to mechanical changes. Vibration and air turbulence were reduced to insignificant levels. Even though this represents excellent stability for a large labora-tory setup, considerable improvement was required, i.e., some form of control or "fringe guiding."

The technique consists of manually correcting any slow drift observed in the moire pattern the interferometer fringes and a dual-frequency grating on a photographic plate located at the exposure plane. By this means, the interferometer was controllable to approximately 1/10 wave for an indefinitely long exposure time. The additional benefit of this technique is excellent repeatability. The same number and orientation of moire fringes will produce an identical grating on subsequent exposures. It is not required that theodolites and sophisticated alignment equipment be used for each exposure. Once a preci-sion reference grating is obtained on the photographic plate, it can be reproduced very accurately in a simple fashion.

In practice, a hole is cut in the reference grating so that the moire fringes are observed around the periphery while the exposure on the metal substrate is taking place.

3.4.2 Reference Grating Fabrication

The reference grating is a transparency on a photographic plate. It is produced using the same process interferometer used to expose the photoresist. In use, it is mounted parallel to the surface of the substrate being exposed, therefore, if its component gra-tings are well aligned, the same will be true of the pattern exposed in the photoresist. Likewise, the frequency ratio on the reference grating will be transferred into the pho-toresist, except for a small correction depending on the number of fringes used in guiding.

It is shown in Appendix F that skew between the gratings is dependent on: (1) align-ment between the rotary table rotation axis and the plane of the surface (in this case the photographic plate) to be exposed and (2) alignment between the rotation axis and the interference fringes. These alignments are carefully performed just prior to exposing a reference grating. The surface alignment is performed by viewing a plane-parallel glass

22

plate mounted in the interferometer's kinematic plateholder with a theodolite and rotating the table through 180°. A high-resolution tilting stage between the rotary table and the plate is adjusted until the plate has the same elevation at 0 and 180° azimuth. The fringe alignment is accomplished by viewing the fringes formed on a mounted reference grating at 0 and 180°. The interferometer fringes are adjusted together with the orthogonal roll axis on the high-resolution tilting stage until vertical fringes are seen in both orientations.

Transparencies produced using the above procedure have been examined with an optical microscope as a coarse test of their alignment. Alignment better than the sensitivity of this test (i.e., better than 100 μrad) has been observed.

The frequency ratio is, of course, governed by the rotary table rotation angle, but is also dependent on the plate's initial alignment normal to the bisector of the interferometer beams. This is accomplished by aligning the rotary table so that when a mirror is held in the plateholder, each interferometer beam returns along the other's incident path. Diffracted-order angle measurements (Section 4.2) have shown that small residuals in frequency ratio can be achieved.

Fringes produced by the reference grating can be observed on the grating itself if developed to a density of about 1. Although the beams diffracted by the grating interfere elsewhere in front of the grating, they overlap with other compound orders and can be difficult to view. Fringe projection at the grating plane has been achieved at both frequencies and provides a usable guiding input.

3.5 DEVELOPMENT PROCESS

Development is the wet chemical process by which the latent exposure in photoresist becomes a relief pattern. It is the same exposure-dependent etching process used in microcircuit fabrication, modified to achieve a known (and as linear as possible) etch-depth versus exposure characteristic.

Linearity can be achieved in any number of ways by using different developer formulations, dilutions, and development times. A process developed during the initial phases of this work gave excellent linearity. Another linear process using a completely different developer was tried later and found to offer deeper relief per unit exposure.

The details of the development process that yield linearity are complex. Empirically, the characteristic has a "toe" analogous to the D-log E curve in photography, followed by a linear region. A uniform preexposure serves to push the latent grating exposure up off the toe. This exposure can be performed with a UV lamp and requires neither the time nor environmental stability of the process interferometer.

So long as the substrate is submersible, the development process appears to be scalable without difficulty to larger substrate sizes.

3.6 ION MILLING

The ion-milling operation transfers the phase relief in the overlying coating into the nickel substrate by sputtering, i.e., removal of material one molecule at a time by the

23

argon ions in the incident beam. The principal difference between the final relief pattern and the original one is a scale factor equal to the ratio of the ion beam etching rates for photoresist and nickel. The presence of an intervening antireflection coating does not affect the scale factor, but merely prolongs the total processing time somewhat.

Because the process is not readily undone to permit additional trials, ion milling was not attempted until late in the project so the earlier steps could be perfected. A preliminary test was performed with an early contact-printed substrate, and indicated that the relative etch rates were nearly equal.

Tests done on directly exposed photoresist gratings later in the program did not confirm this result but showed that the relative etch rate can be a critical function of the ion beam accelerating potential and the ion beam current. Not all the mechanisms for these dependences are known, but it is clear that the higher beam currents cause a significant amount of substrate heating. This is known to introduce plastic flow in photoresist and hence a reduction in the amplitude of the phase relief. This is consistent with the observation that the final modulation achieved in metal was significantly less than that achieved in photoresist.

Two finished gratings were ion-milled. These were dual-frequency operational designs. The groove depths were in one case shallower and in the second case deeper than their design values. As the details of the ion-milling process are further understood, the target modulation can more accurately be achieved, as exposure and development can be varied to compensate for the established etch rate ratio.

3.7 FABRICATION TRIALS

In the course of this program, 29 direct holographic exposure/fabrication cycles were conducted, characterized, and documented. Table 3-1 summarizes these trials chronologically.

The first six trials were process calibration tests to establish the groove depth as a function of exposure and development. During these it became clear that fringe drifts could not be completely eliminated from the process interferometer and the manual guiding technique was introduced. At the same time, the exposure wavelength was changed to $\lambda = 0.4880$ μm since the increased power available at this wavelength more than compensated for the loss in photoresist spectral sensitivity.

With the adoption of this exposure wavelength, an antireflection coating was designed to suppress reflections at the photoresist-metal interface. Two of the substrates were so coated and were used extensively in the remaining tests. Five of the early trials were performed on quartz substrates to index-match the photoresist as a control test of the effects of standing waves. These were inconclusive chiefly because of the failure of developed photoresist to adhere to the quartz.

After four additional calibration attempts (through 19 March 1981) spin-coating of photoresist was introduced because of difficulty achieving consistent uniformity with dip-coating. After three more calibration trials, dual-frequency exposures were attempted to fabricate a boresight demonstration grating. A number of these resulted in groove profiles that were "bottomed out" because the depths required for an efficient demonstration

24

grating were greater than the photoresist thickness produced by spin coating. Two calibration exposures to test whether this apparent phenomenon was in fact the result of offset preexposure were inconclusive.

It was learned that another developer formulation (AZ-303A) offered greater groove depth, and hence it was substituted to relax the exposure duration. A usable demonstration grating was fabricated.

The last four trials were dual-frequency gratings with operational groove depths and frequency ratios. Two of these were ion-milled to yield finished gratings.

Table 3-1 -- Fabrication Trial Summary

Date	Substrate	Photoresist	Exposure	Development	Remarks
4 Dec 80	Ni	Dip-coated	λ = 458 nm (>3 hr)	AZ-606	Single-frequency exposure calibration
7 Dec 80	Ni	Dip-coated	54; 72; 90 mJ/cm^2	AZ-606	
13 Dec 80	Quartz	Dip-coated	54; 108 mJ/cm^2	AZ-606	
18 Dec 80	Quartz	Dip-coated	30; 68 mJ/cm^2	AZ-606	
22 Dec 80	Quartz	Dip-coated	36 mJ/cm^2	AZ-606	
16 Jan 81	Quartz	Dip-coated	22 mJ/cm^2	AZ-606	
19 Jan 81	Quartz	Dip-coated	λ = 488 nm 2,400 mJ/cm^2	AZ-606	Change to λ = 488 nm, introduced manual guiding
21 Jan 81	Ni/ARC*	Dip-coated	630 mJ/cm^2	AZ-606	
23 Jan 81	Ni	Dip-coated	1,260 mJ/cm^2	AZ-606	
19 Mar 81	Ni	Dip-coated	2,500 mJ/cm^2	AZ-606	
25 Mar 81 (A)	Ni/ARC	Spin-coated	3,000 mJ/cm^2	AZ-606	Introduced spin coating
25 Mar 81 (B)	Ni/ARC	Spin-coated	NA†	AZ-606	
26 Mar 81	Ni/ARC	Spin-coated	NA	AZ-606	
29 May 81	Ni/ARC	Spin-coated	NA	AZ-351	Dual-frequency exposure (demonstration design)
1 Jun 81	Ni	Spin-coated	1,800; 1,800 mJ/cm^2	AZ-606	
2 June 81	Ni/ARC	Spin-coated	1,600; 990 mJ/cm^2	AZ-606	
5 June 81	Ni/ARC	Spin-coated	1,100; 1,100 mJ/cm^2	AZ-606	
8 June 81	Ni	Spin-coated	360; 360 mJ/cm^2	AZ-606	

Table 3-1 -- Fabrication Trial Summary (Cont.)

Date	Substrate	Photoresist	Exposure	Development	Remarks
11 June 81	Ni/ARC	Spin-coated	700; 770 mJ/cm^2	AZ-606	
22 June 81	Ni	Spin-coated	300; 700; 1,100 mJ/cm^2	AZ-606	Single-frequency exposure calibration
24 June 81	Quartz	Spin-coated	340, 680, 1,020 mJ/cm^2	AZ-606	Single-frequency exposure calibration
10 July 81	Ni/ARC	Spin-coated	1,000; 1,000 mJ/cm^2	AZ-606	Dual-frequency, demonstration design
14 July 81	Ni	Spin-coated	780; 120 mJ/cm^2	AZ-606	Dual-frequency, operational design
16 July 81	Ni	Spin-coated	300; 670; 1,000 mJ/cm^2	AZ-303A	Single-frequency exposure calibration
20 July 81	Ni/ARC	Spin-coated	730; 230 mJ/cm^2	AZ-303A	Final product used in boresight demonstration experiment
24 July 81 (A)	Ni/ARC	Spin-coated	190; 54 mJ/cm^2	AZ-303A	Dual-frequency operational ion-milled
26 July 81 (B)	Ni/ARC	Spin-coated	150; 42 mJ/cm^2	AZ-303A	Used in ion-milling calibration tests
26 July 81	Ni/ARC	Spin-coated	150; 42 mJ/cm^2	AZ-303A	Ion-milling candidate (not milled)
14 Sept 81	Ni/ARC	Spin-coated	475; 128 mJ/cm^2	AZ-303A	Final product: ion-milled operational grating

*ARC = antireflection coating
†NA = not available

26

4. PARAMETER CHARACTERIZATION AND CONTROL

Parameter measurements serve two purposes: (1) to test the finished gratings conformity to design specification and (2) to perform intermediate process control. The parameters characterized are groove depths, frequencies, frequency ratio, skew between frequencies, diffracted wavefront quality and optical surface quality. The skew and frequency ratio are determined by the quality of the reference grating used in the process interferometer, as mentioned in Section 3.4.3. These measurements have chiefly been performed on the reference grating, although their measurement on the final product is also possible and, of course, important.

The processes that precede ion-milling are readily "retraceable" since a photoresist coating can be easily stripped from the substrate. Restoring an ion-milled substrate, however, would be far more difficult. Thus, intermediate parameter and quality control measurements allow for multiple process trials before ion-milling. This is especially crucial where the substrate is expensive and only one copy exists. Although substrate costs or uniqueness was not a driving consideration during this fabricability program, it is an issue the parameter measurement task has addressed.

4.1 DIFFRACTED-ORDER INTENSITIES/GROOVE DEPTH DETERMINATION

Diffracted-order intensity measurements were performed in order to test developed photoresist gratings prior to ion-milling as a final inspection of ion-milled substrates. These measurements yield efficiencies from which groove depths are calculated.

All measurements were made with either a helium-neon or an argon ion laser. The raw beam was directed to a single spot on the grating and the power in all significant (i.e., not negligibly bright) orders was measured with a radiometer. Generally both positive and negative diffraction orders were measured and an extra measurement of the zero-order performed. The additional data checked for drifts in laser power and overall measurement consistency. By measuring a single spot (~2-mm diameter) on the grating, the technique is relatively insensitive to variations in groove depth that can occur across an expanded beam.

The approach to the groove depth determination is to use scalar diffraction theory (Section 2.2). This is generally valid for depths up to 0.2 μm at the 5-μm period of the GBC. The measured intensities are normalized by their aggregate sum, yielding the efficiency ϵ_n of the n-th order. From math tables the argument of the corresponding Bessel function J_n whose square equals ϵ_n is determined. The groove depth is $\lambda/2\pi$ times the argument.

Performing this for several orders provides independent determinations to resolve ambiguities when more than one argument of a given order of the Bessel function yields the measured efficiency. Lack of consistency among the multiple solutions generally indicates a nonsinusoidal profile, due to developing through the photoresist in the groove troughs.

A summary of groove depth values in photoresist is given in Table 4-1. Groove depths for ion-milled gratings appear in Table 4-2.

4.2 MEASUREMENT OF FREQUENCIES

The accurate measurement of frequencies permits the determination of the grating frequency ratio, a critical specification. The frequencies are individually derived from angular measurements of the diffracted orders generated by the grating when illuminated with a collimated laser beam. These measured angles and their corresponding order numbers are used to obtain λ/d by linear regression on the grating equation.

The frequency ratio measurement is performed on reference grating transparencies to eliminate a gross deviation from the target ratio and to establish the magnitude and sign of the residual. To establish a level of precision for this measurement procedure, it was repeated six times on a transparency that was later used as a reference grating. A breakdown of these data appear in Table 4-3. The standard deviation of the resulting values of d_2/d_1 is 1.7×10^{-4}. The precision of this technique at this reporting is limited by distortion of the diffracted wavefronts by imperfections in the transparencies themselves. As unwanted artifacts are eliminated from the exposure process, more precise theodolite readings will be possible, resulting in reduced uncertainty in the frequency ratio. A calculation of expected uncertainty in the frequency ratio assuming resolution no finer than (λ/D) where D is the theodolite aperture, is given in Appendix G. The predicted value of 1.3×10^{-4} is in reasonable agreement with the standard deviation of the above measurements.

The ratio measurement can ultimately be performed on developed photoresist gratings as an inspection that must be passed prior to ion-milling.

4.3 GRATING SKEW MEASUREMENTS

The skew between grating frequencies is a specification critical to the performance of the GBC. As discussed in Section 2.3, small values of skew introduce an offset between wavefront sensor beams that is independent of the angle of incidence. There is no design (i.e. choice of frequency ratio) that will produce co-boresighted sample beams (see Appendix H). To ensure that skew is small enough and to predict the offset, it must be measured.

Two measurement techniques were developed on this program. The first uses a microscope with a horizontal translation stage. The surface of the grating being measured is examined and the two grating frequencies observed. The grating is translated parallel to the groove direction and the drift (in fractions of a fringe) is noted over a total excursion of 50 mm. This technique has been used extensively to test reference gratings. The limiting skew that can be detected is approximately 100 μrad.

28

Table 4-1 -- Photoresist Groove Depth Summary

Date	Depth(s), μm
4 Dec 80	NA*
17 Dec 80 (A)	0.08, 0.06, 0.03 (one frequency, three exposure durations)
13 Dec 80	No grating
18 Dec 80	0.0015, 0.005 (one frequency, two exposure durations)
22 Dec 80	NA
16 Jan 81	0.054
19 Jan 81	0.17
21 Jan 81	0.16
23 Jan 81	0.2
19 Mar 81	NA
25 Mar 81 (A)	NA
25 Mar 81 (B)	0.2
26 Mar 81	0.3
29 May 81	NA
1 June 81	NA
2 June 81	0.06, 0.06 (two frequencies)
5 June 81	0.3 (5.000-μm grating)
8 June 81	0.07, 0.02
11 June 81	0.07, 0.05 (two frequencies)

Table 4-1 -- Photoresist Groove Depth Summary (Cont.)

Date	Depth(s), μm
22 June 81	0.04, 0.08, 0.12 (one frequency, three exposure durations)
24 June 81	0.05, 0.12 (one frequency, two exposure durations)
10 July 81	0.03, 0.07 (two frequencies)
14 July 81	0.008, 0.004 (two frequencies)
16 July 81	0.3, 0.4, 0.5 (one frequency, three exposure durations)
20 July 81	0.50, 0.14 (two frequencies)
24 July 81	0.13, 0.05
26 July 81 (A)	0.1, 0.04
26 July 81 (B)	0.1, 0.03
14 Sept 81	NA

*NA: not available

Table 4-2 -- Ion-Milling Groove Depth Summary

Date	Depth in Photoresist, μm	Depth in Nickel, μm	Ion Beam Incidence Angle, degrees	Grating Period, μm
24 July 81	0.13	0.05	NA*	5.00
	0.05	0.02	NA	5.33
26 July 81 (A)	0.09	0.008	35	5.00
	0.04	0.04	40	5.00
	0.10	0.02	50	5.00
	0.08	0.02	45	5.00
	0.04	0.010	35	5.33
	0.12	0.010	40	5.33
	0.3	0.006	50	5.33
	0.3	0.006	45	5.33
14 Sept 81	NA	0.2	NA	--
		0.05	NA	--

*NA: not available

31

Table 4-3 -- Frequency Ratio Measurements, Transparency No. 49

$$\langle d_2/d_1 \rangle = 1.18584 \quad \sigma / d_1/d_2 = 0.00017$$

m_1	m_2	θ	d_2/d_1	m_1	m_2	θ	d_2/d_1
1	0	5° 36' 20"		1	0	5° 36' 00"	
2		11 15 33		2		11 14 54	
3		17 01 40		3	↓	17 00 45	
4		22 58 17	1.18560	4		22 57 17	1.18578
0	1	4 43 21		0	1	4 43 10	
	2	9 28 25			2	9 27 58	
	3	14 17 45			3	14 16 58	
↓	4	19 13 08		↓	4	19 12 09	
1	0	5° 35' 41"		1	0	5° 35' 43"	
2		11 14 59		2		11 14 41	
3		17 00 57		3		17 00 38	
4		22 57 23	1.18571	4		22 57 31	1.18593
0	1	4 43 14		0	1	4 42 58	
	2	9 27 53			2	9 27 51	
	3	14 17 12		3		14 16 57	
↓	4	19 12 28		↓	4	19 12 08	

Table 4-3 -- Frequency Ratio Measurements, Transparency No. 49 (Cont.)

$\langle d_2/d_1 \rangle$ = 1.18584 $\sigma/d_1/d_2$ = 0.00017

m_1	m_2	θ			d_2/d_1	m_1	m_2	θ			d_2/d_1
1	0	5°	35'	35"		1	0	5°	35'	45"	
2		11	14	32		2		11	14	42	
3		17	00	18		3		17	00	48	
4		22	57	15	1.18589	4		22	57	37	1.18612
0	1	4	42	42		0	1	4	43	02	
	2	9	27	29			2	9	27	46	
	3	14	16	39			3	14	16	55	
	4	19	11	54			4	19	12	05	

The second technique uses the grating under test to generate a shearing interferogram. This is done by focusing a laser beam at the grating surface and viewing the fringes produced (see Fig. 4-1). The fringe density can be varied by adjusting the focus. The two grating frequencies will generate two superimposed fringe patterns, whose alignment can be examined visually. To achieve adequate measurement sensitivity the grating can be translated along the groove direction and a given pair of fringes tracked. The interferogram produced by this method is shown in Fig. 4-2.

The sensitivity of any skew measurement scheme will be inversely proportional to the length of the grating to be tested. The smallest detectable skew will be of the order of one groove width divided by the "run" or length of the groove. Obviously smaller skews can be measured on larger gratings.

4.4 OPTICAL QUALITY

There are two aspects to the optical quality of a reflecting diffraction grating, surface figure and groove figure. The GBC is a plane grating so the figure should be flat and the grooves straight and parallel. Interferometry is used to measure both.

Surface interferometry can be conveniently performed at any step in the fabrication process. Since the interferometer uses HeNe lasers testing can be done even on unexposed photoresist coatings. In practice, surface interferometry is used to examine coating uniformity as well as the flatness of uncoated and ion-milled substrates. Interferograms of typical gratings at various stages of fabrication are shown in Figs. 4-3 and 4-4. Interferograms taken after photoresist coating but prior to exposure are in Fig. 4-8. These indicate an optical figure flat to within $\lambda/8$ peak-to-peak both before and after the exposure/development cycle for two samples fabricated and tested late in program.

Groove straightness can be tested using the process interferometer to reconstruct the original beams that recorded the grating and combining them so as to interfere at a fringe density appropriate to optical testing (see Fig. 4-5). This is more conveniently done using a transparency rather than the actual substrates, since the fringes can be viewed in transmission. Figure 4-6 shows an interferogram recorded in this manner, characterizing the quality of the process interferometer (and equivalently the groove straightness). This was done prior to a recoating of the 12.5-in. beam splitter used in the interferometer after which it displayed $\sim 1\lambda$ departure from flatness.

4.5 ELECTRON MICROSCOPY

Though not routinely performed on this fabricability program, electron microscopy is a useful tool for studying groove profiles directly. Though it can be done without harming an all-metal sample, it can ruin a photoresist coating and is incapable of being done on samples that are too large.

To avoid these difficulties, miniature epoxy replicas were made of an aluminized single-frequency grating in photoresist. These $1/4$-in.-diameter replicas were coated with gold and examined with a scanning electron microscope (SEM). Figure 4-7 is an electron micrograph of a replica made of a single-frequency grating.
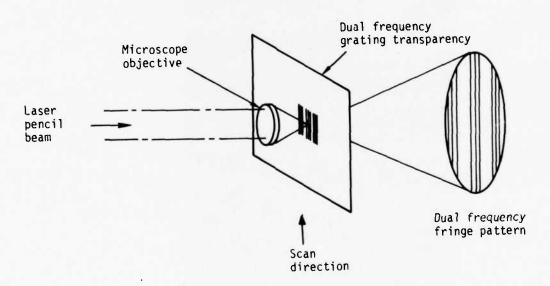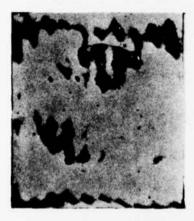
Fig. 4-1 -- Interferometer grating skew measurement

Fig. 4-2 -- Grating skew interferogram

(a) Sample no. 1   (b) Sample no. 9

(c) Sample no. 4

Fig. 4-3 -- Interferograms of substrates after exposure and development
of photoresist

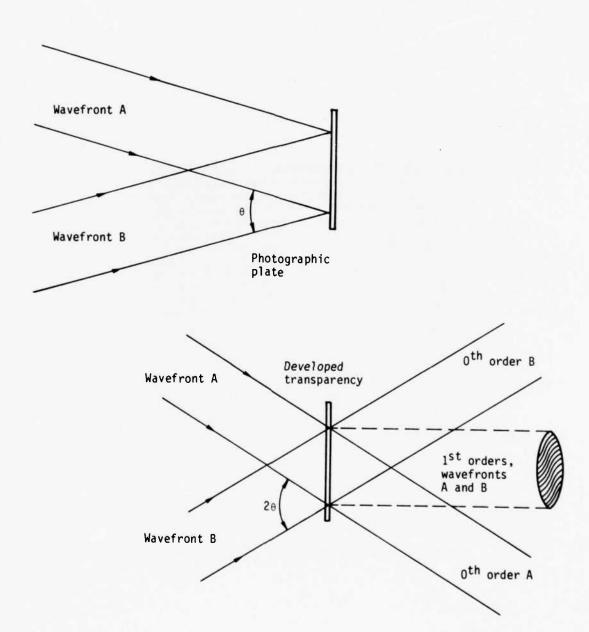(a) Sample no. 4

(b) Sample no. 2

Fig. 4-4 -- Interferograms of ion-milled gratings

Fig. 4-5 -- Arrangement for recording interferogram of grating groove quality
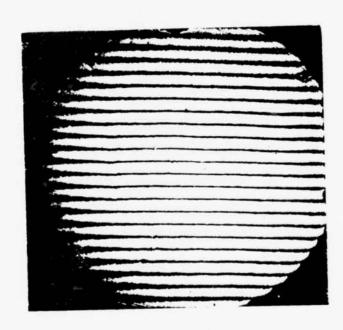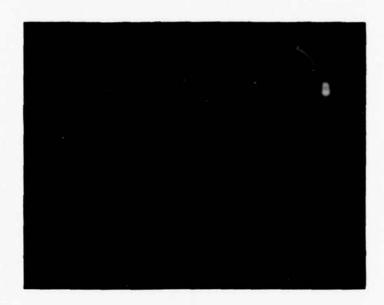
Fig. 4-6 -- Interferogram of process interferometer beams

Fig. 4-7 -- Electron micrograph of grating replica

4.6 FILM MEASUREMENTS

The critical dependence of the overall grating fabrication process on photoresist coating quality dictates a requirement for measurements of the film itself. An effort was made to explore techniques that are nondestructive and do not otherwise compromise the process.

Ordinary interferometry of a photoresist-coated sample can be performed to yield an optical path difference (OPD) profile of the coating in transmission. As previously mentioned, the helium-neon wavelength does not further expose the photoresist.

Figure 4-8 shows two interferograms of samples with photoresist coatings prior to exposure with the process interferometer. The brightness of the test beam is very sensitive to slight variations in film thickness, as seen in sample number S/N 9.
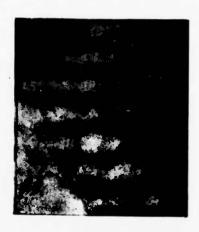
Figure 4-9 shows how specific coating process deficiencies are revealed interferometrically. The left-hand sample was dip-coated and exposed through a mask with six rectangular regions. Aside from the steps associated with the mask, there are lap features that result from an insufficiently stable dip-coating cycle. The right-hand sample illustrates the "stringing" phenomenon that can take place during a spin-coating cycle.

Measurement of the height of a step in the film is frequently useful to calibrate an etching process or to determine the thickness of a coating through which a step has been etched. Though this might be attempted using the same interferometer, the sharpness of an actual step frequently makes it impossible to resolve a fringe ambiguity.

A white light interference microscope has been used to overcome this difficulty (see Fig. 4-10). The microscope focuses the white light source onto the sample through a semitransparent beam splitter in contact with the sample surface. The beams reflected from the sample and the beam splitter return through the microscope and their interference is observed visually through a prism. Dark fringes are seen at each wavelength for which the OPD between the film surface and the beam splitter are an odd number of half wavelengths. The wavelengths at which the dark fringes occur are measured using a calibrated reticle. By measuring these on both sides of a film step, the OPD across the step can be determined.

A qualitative film thickness profile can be obtained by illuminating the coated sample with a single collimated beam and visually observing the footprint of the reflected beam while continuously varying the angle of incidence using a rotary table. The brightness varies with angle due to interference in the film. The angular position of the nulls are a function of film thickness.

A routine technique for film measurements is the use of a profilometer (Dektak) to obtain quantitative information on surface profile. The Dektak monitors the vertical motion of a stylus transducer as the sample is transported beneath it. The validity of the stripchart data trace thus generated (see Fig. 4-11) depends on the hardness of the film. Unbaked photoresist is sufficiently soft that the stylus can plow into it, and the depth of a step may not be accurately reproduced. Nevertheless, the Dektak does provide an unambiguous and convenient measure of surface profile, both for hard films and ion-milled substrates.
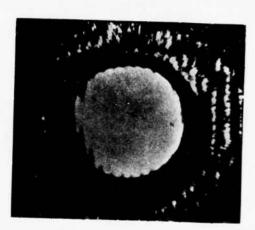
(a) Sample no. 1   (b) Sample no. 9

Fig. 4-8 -- Interferograms of unexposed photoresist coatings

(a) Horizontal "lapping"
(dip coating)

(b) Radial "stringing"
(whirl coating)
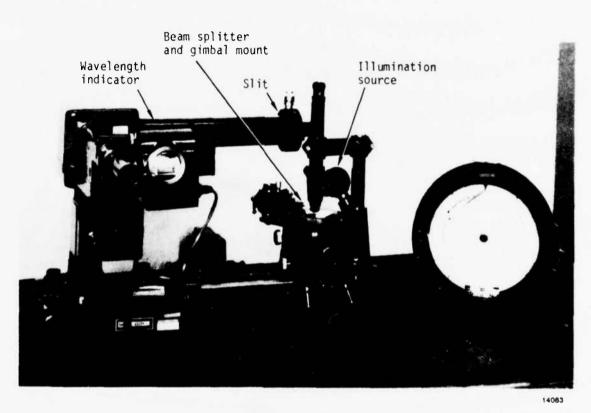
Fig. 4-9 -- Coating process artifacts
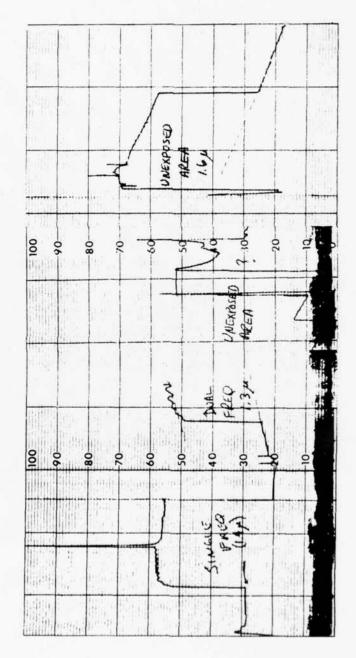
44

Fig. 4-10 -- White light interference microscope

Fig. 4-11 -- Profilometer traces

5. BORESIGHT DEMONSTRATION EXPERIMENT

The boresight demonstration experiment was performed to verify the use of the dual-frequency grating as a two-wavelength beam combining instrument. A demonstration grating was designed for this purpose with the frequency ratios and modulation depths adjusted to fit the experiment. Using 0.6328 and 3.39 μm helium-neon lasers required a frequency ratio of 1.1866, which was achieved with grating periods of 5.0 and 5.933 μm. The orders m,n, and p discussed in Section 2.1 are (1,1,1) for this grating. Therefore, the modulation depths were adjusted to give high efficiencies in the first-order. Peak-to-peak depths of 0.13 μm were chosen for each grating. The grating was aluminized instead of being ion-milled.

The experiment was set up as illustrated in Figs. 5-1 and 5-2. Figure 5-3 indicates how the boresighting was actually detected. The visible corner cube was positioned to receive the (0,0) order, which yields counterpropagating visible and infrared beams. The infrared corner cube received its (1,0) order, where the first value corresponds to the 5.933-μm frequency and the second to the 5.0-μm. Both beams were sent back onto the grating and the (1,0) visible and (0,1) infrared orders were picked up at the detector. Tip-tilt adjustment on the mirrors and beam splitter allowed for the fine adjustments necessary for alignment. Two germanium beam splitters with an antireflection coating for 3.39 μm were used to initially combine the beams and to separate them for detection.

The first step of the experiment was to verify the beams were initially boresighted. This was done by placing a plane mirror in the beam path before it strikes the grating and sending the beams onto the focusing mirror and detector system. Once this alignment was achieved the corner cubes could be accurately located and the diffracted beams' boresighting detected. It was noticed, however, that shutting down the system affected the alignment. Therefore, all measurements had to be made consecutively.

In order to detect boresighting, the outputs of a silicon photodiode and a lead-selenide detector were connected to an oscilloscope. The boresighted beams were chopped at 400 Hz. The infrared signal was then sent through a narrow-band filter to reduce the background effects. Tests were conducted in subdued light to reduce the visible background. The slit was translated by means of a micrometer until a maximum signal was located on the oscilloscope. The micrometer readings for each beam's maximum was recorded with their difference representing the boresight error. The width of the slit was adjusted to give the sharpest maxima without substantially reducing the signal.

The error (millimeters) can be converted to angle by taking the inverse tangent of this difference divided by the focal length of the mirror in millimeters

$$\theta = \tan^{-1}\left(\frac{|X_{ir} - X_{vis}|}{f}\right)$$

For this experiment a parabolic mirror with focal length of 44 in. was used to focus the beams onto the slit.

The accuracy with which the maxima can be located represents the limiting factor in the accuracy of the boresight measurements. Measurements were made at a minimum of five times and averaged. The standard deviation of these values represents the uncertainty in the maxima. It was found that these maxima could be located to within 0.01 mm horizontally and 0.02 mm vertically. This represents a tolerance of 2 arc-sec and 4 arc-sec respectively in the results. The visible beam was slightly more precise than the infrared, but not enough to sufficiently affect the tolerances. Tests were conducted in both the vertical and horizontal planes at two different incident angles. The initial measurements were made at 40° incidence as this represented a convenient optical layout.

It was found the boresighting occurred in both planes to within the tolerances of 2 and 4 arc-sec. The grating was then rotated by 2° to achieve a new incidence angle of 38°. Boresighting also occurred at this angle to within these tolerances. Data from this experiment is shown in Table 5-1.

Errors were introduced in the initial beams' alignment and the resulting errors in the diffracted alignment were measured. Results show that for small offsets, on the order of 1 mm or less, the diffracted beams' displacements were directly proportional to the incident beams. The experimental data are plotted in Figs. 5-4 and 5-5. As the initial offsets increased, the final offsets became less linear. This is most likely due to the detector system and its limited field of view. The detector elements were 2 mm^2, so offsets of greater than this were difficult to detect.

It does appear, however, that to within the experimental limits, the dual frequency grating is successful as a boresighting device and is insensitive to rigid body motions of the grating.

Table 5-1 -- Boresight Invariance With Respect to Angle of Incidence

Input alignment	ΔX_{VIS-IR}	θ_{VIS-IR}
Horizontal plane	0.003 mm	(0.6 arc-sec)
Vertical plane	0.010 mm	(1.8 arc-sec)
Output boresighting		
Horizontal Plane		
40° incidence	0.001 mm	(0.2 arc-sec)
Rotated to 38° incidence	0.009 mm	(1.7 arc-sec)
Vertical plane		
40° incidence	0.011 mm	(2 arc-sec)

Detectors

3.39 μm
laser

Chopper

f = 44 in.

Grating

Dichroic
beam splitter

Corner
cube

IR

Visible

0.6328 μm
laser
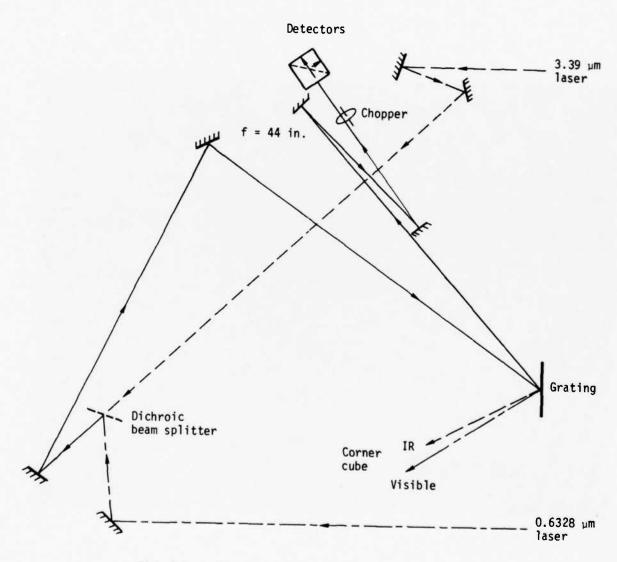
Fig. 5-1 -- Boresight demonstration experimental setup

49

27456
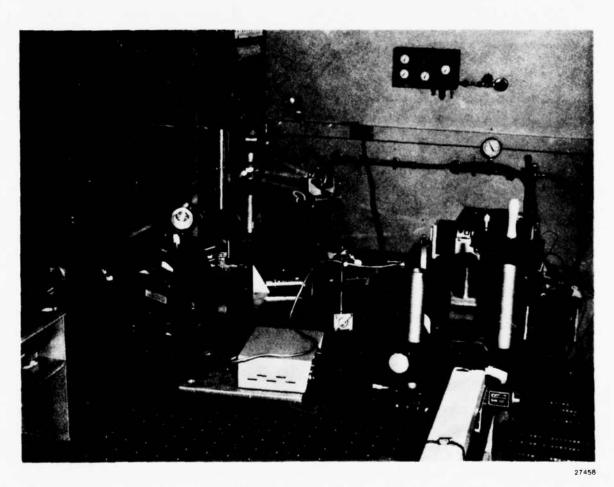
Fig. 5-2 — Boresight demonstration experiment apparatus

To oscilloscope

Narrow
waveband
filter and
amplifier

Adjustable
slit

Chopper
(400 Hz)

PbSe
(infrared)

Silicon
(visible)
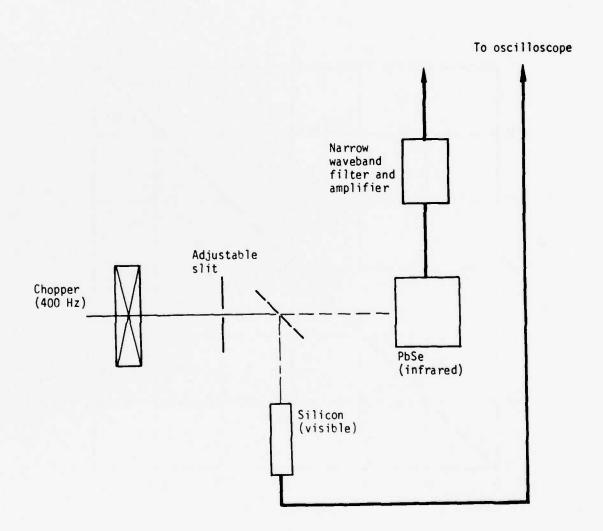
Fig. 5-3 -- Boresight demonstration detector arrangement

51

Expected
results

1.2

1.046
1.055

1.0

0.8

Output Offset, mm

0.6

0.505
0.510

0.4

0.265
0.258

1 mm = 185 arc-sec

0.2

0

0   0.2   0.4   0.6   0.8   1.0   1.2

Input Offset, mm
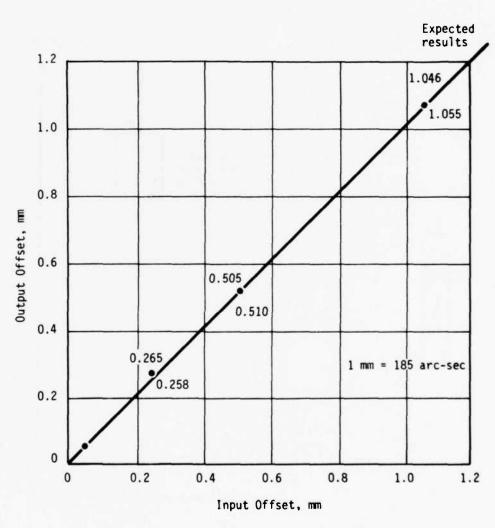
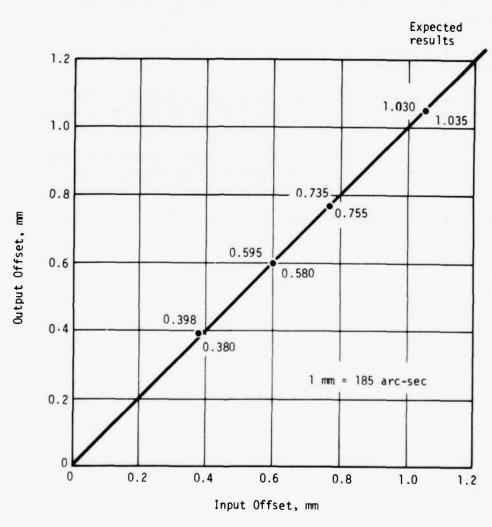Fig. 5-4 -- Horizontal boresight response

Fig. 5-5 -- Vertical boresight response

53

6. CONCLUSIONS

The fabricability and performance of the grating beam combiner (GBC) have been validated by this program:

1. Fabrication through the ion-milling stage yielded two scaled operational gratings.

2. The direct exposure process was substituted for contact printing. It yields a high-quality, low-scatter grating and is scalable to larger substrate sizes.

3. The boresighting performance of the GBC was demonstrated with a high-efficiency grating fabricated by the same processes, with a frequency ratio scaled for surrogate wavelengths.

4. The gratings were characterized as to:

     - Groove depth
     - Frequency ratio
     - Surface figure
     - Diffracted wavefront quality
     - Inter-grating skew

   The parameter characterization methods can be scaled to accommodate larger substrates.

5. Analysis of tolerances peculiar to the GBC have indicated how its performance depends on skew and frequency ratio residual.

If the system pointing tolerance is assumed to be one-fifth of an Airy disk (λ = 2.7 μm), the required GBC boresighting accuracy is 0.27. Accuracy of 2 arc-sec was demonstrated with a relatively unsophisticated detection system working with a 1.2-cm beam diameter. No difficulty is anticipated in meeting the 0.27 arc-sec requirement with a larger beam diameter (approximately 20 cm) and the precision boresight detection scheme.

Appendix A

GENERALIZED GBC DESIGN EQUATION

A more general approach to the grating beam combiner treats each diffraction as a compound order from the two frequencies. The grating equations are

$$\sin \theta_1 + \sin \theta_2 = m_1 \lambda_{IR} f_1 + m_2 \lambda_{IR} f_2$$

$$\sin \theta_2 + \sin \theta_{IR} = n_1 \lambda_{IR} f_1 + n_2 \lambda_{IR} f_2$$

$$-\sin \theta_1 + \sin \theta_{UV} = p_1 \lambda_{UV} f_1 + p_2 \lambda_{UV} f_2$$

The resulting frequency ratio solution is

$$\frac{f_2}{f_1} = \frac{(m_1 - n_1)\lambda_{IR} + p_1 \lambda_{UV}}{(n_2 - m_2)\lambda_{IR} - p_2 \lambda_{UV}}$$

For $m_2 = n_1 = p_2 = 0$, this reduces to the frequency ratio formula in Section 2.1.

55

BORESIGHT ERROR FORMULAS

1. Boresight Error Due To Frequency Ratio Residual

From the combined grating equations (in Section 2.1),

$$\sin \theta_{UV} - \sin \theta_{IR} = m\lambda_{IR} f_1 - n\lambda_{IR} + p\lambda_{UV} f_1$$

A trigonometric identity changes the left-hand side to

$$2 \sin\left[\frac{(\theta_{UV} - \theta_{IR})}{2}\right] \cos\left[\frac{(\theta_{UV} + \theta_{IR})}{2}\right] = \ldots$$

Assuming $\theta_{UV} \approx \theta_{IR}$

$$\Delta\theta \cos\theta_{IR} = \left[m\lambda_{IR} - n\lambda_{IR} \left(\frac{f_2}{f_1}\right) + p\lambda_{UV}\right] f_1$$

$$\Delta\theta = \frac{f_1 n\lambda_{IR}}{\cos\theta_{IR}} \left\{\frac{m\lambda_{IR} + p\lambda_{UV}}{n\lambda_{IR}} - \frac{f_2}{f_1}\right\}$$

The terms brackets is the difference, $\delta(f_2/f_1)$, between the design frequency ratio, FR, and the actual frequency ratio. Hence,

$$\Delta\theta = \frac{f_1 n\lambda_{IR}}{\cos\theta_{IR}} \delta\left(\frac{f_2}{f_1}\right)$$

2. Boresight Error Due To Input Beam Misalignment

Rewritten to allow for the angular difference, the first two grating equations are

$$\sin\theta_1 + \sin\phi = m\lambda_{IR} f_1$$

$$\sin\phi + \sin\theta_{IR} = n\lambda_{IR} f_2$$

$$\sin(-\theta_2) + \sin\theta_{UV} = p\lambda_{UV} f_1$$

Combining and using the trigonometric identity yields

$$(\sin \theta_1 - \sin \theta_2) + (\sin \theta_{UV} - \sin \theta_{IR}) = m\lambda_{IR}f_1 - n\lambda_{IR}f_2 + p\lambda_{UV}f_1$$

$$\Delta\theta_i \cos \theta_i + \Delta\theta_{UV-IR} \cos \theta_{IR} = f_1 n\lambda_{IR}FR - n\lambda_{IR}f_2$$

$$= f_1 n\lambda_{IR} \left(FR - \frac{f_2}{f_1}\right)$$

$$= f_1 n\lambda_{IR} \, \delta\left(\frac{f_2}{f_1}\right)$$

Hence

$$\Delta\theta_{UV-IR} = \left(\frac{\cos \theta_i}{\cos \theta_{IR}}\right)\Delta\theta_i + \left(\frac{f_1 n\lambda_{IR}}{\cos \theta_{IR}}\right)\delta\left(\frac{f_2}{f_1}\right)$$

Appendix C

ANTIREFLECTION COATING FOR NICKEL

A coating has been designed for use under the photoresist that nearly eliminates the light reflected from nickel at one wavelength (0.488 μm). The coating gives a reflection of 3% or less, even allowing for a reasonable thickness tolerance.

The coating can be considered to be two coatings: (1) a layer on top of the nickel that has the effect of making the apparent index of refraction "real," i.e., with no absorption coefficient, and (2) two layers to antireflect that apparent index. This gives a total of three layers. The complex index of refraction of nickel is about $(1.5 - 2.8 j)$ at $\lambda = 0.488$ μm. It has a reflectance of 55% in air. Under the photoresist (n = 1.65) the nickel has a reflectance of 48%. A thin layer [0.61 quarter-wave optical thickness (QWOT) at 0.488 μm] of zinc sulfide (or titanium dioxide) on nickel gives a "real" index of n ≅ 0.5. In air this would give a reflectance of about 11%, but under the photoresist it gives a reflectance of 22%. A single layer to match between 1.55 and 0.5 needs an index of about 0.9--a quarter-wave layer of vacuum or air would be sufficient. For realistic coating materials we need to use two--a layer of magnesium fluoride and a layer of ZnS or TiO_2 will work well. The final design is layered as shown:

Photoresist
1 QWOT ZnS (or TiO_2)
1 QWOT MgF_2
0.61 QWOT ZnS (or TiO_2)
Nickel

The QWOT is 0.488 μm. The analysis indicates that such a coating has a reflectance of 0.2%. The coating without the photoresist has a reflectance of 7%.

The thickness sensitivity needed to obtain a reflectance of 3% or less is about ±15% for the top layer, ±10% for the middle layer, and ±5% for the thin layer next to the nickel. The thickness of the photoresist makes no difference, but the index of refraction makes little difference (the coating should be redesigned if the photoresist has an index of n = 1.50 or less). The photoresist has some relatively weak absorption, but this should make little or no difference.

Appendix D

STANDING WAVE INTENSITY IN PROXIMITY TO A METAL SUBSTRATE

Consider two collimated beams incident on a mirror

$$A_1 \exp(i\vec{\alpha} \cdot \vec{r})$$

$$A_2 \exp(i\vec{\beta} \cdot \vec{r})$$

where α and β are the wavevectors for the two beams. Both have the same wavelength, hence $|\vec{\alpha}| = |\vec{\beta}|$. Reflection reverses one of the components of the wavevector, and can be treated as a length preserving operator, R. For example, if the mirror lay in the XZ plane, the Y component would be reversed

$$R = \begin{pmatrix} 1 & 0 & 0 \\ 0 & -1 & 0 \\ 0 & 0 & 1 \end{pmatrix}$$

The reflected wave amplitudes are

$$A_1 \exp(iR\vec{\alpha} \cdot \vec{r})$$

$$A_2 \exp(iR\vec{\beta} \cdot \vec{r})$$

The intensity of these four interfering beams is

$$I(\vec{r}) = \left| A_1^{i\vec{\alpha} \cdot \vec{r}} + A_1 e^{iR\vec{\alpha} \cdot \vec{r}} + A_2 e^{i\vec{\beta} \cdot \vec{r}} + A_2 e^{iR\vec{\beta} \cdot \vec{\delta}} \right|^2$$

Carrying out the squaring operation and simplifying the expression gives

$$I(r) = 2A_1^2 \left\{ 1 + \cos\left[(\vec{\alpha} - R\vec{\alpha}) \cdot \vec{r} \right] \right\} + 2A_2^2 \left\{ 1 + \cos\left[(\vec{\beta} - R\vec{\beta}) \cdot \vec{r} \right] \right\}$$
$$+ 2A_1 A_2 \left\{ \cos\left[(\vec{\alpha} - \vec{\beta}) \cdot \vec{r} \right) + \cos\left[(\vec{\alpha} - R\vec{\beta}) \cdot \vec{r} \right] \right.$$
$$\left. + \cos\left[(R\vec{\alpha} - \vec{\beta}) \cdot \vec{r} \right] + \cos\left[R(\vec{\alpha} - \vec{\beta}) \right] \cdot \vec{r} \right\}$$

This is a general expression that is valid for beams incident from any direction, including beams in different planes and angles of incidence. More specific expressions can be written for cases where both are in the same plane of incidence or where the normal to the mirror bisects the incident rays.

Inspection of the reduced expression for $I(\vec{r})$ reveals cosine dependence at six different vector spatial frequencies:

$(\vec{\alpha} - \vec{\beta})$: Interference between incident beams at desired grating frequencies, nodal surfaces more or less normal to metal substrate.

$(\vec{R\alpha} - \vec{R\beta})$: Interference between reflected beams, nodal surface more or less normal to metal substrate.

$(\vec{\alpha} - \vec{R\alpha})$, $(\beta - R\beta)$: Interference between each beam and its own reflection, nodal surfaces parallel to the substrate.

$(\vec{\alpha} - \vec{R\beta})$, $(\vec{R\alpha} - \vec{\beta})$: Interference between each beam and the others' reflection.

Appendix E

INTENSITY DISTRIBUTION PRODUCED BY INTERFERENCE BETWEEN
HORIZONTALLY POLARIZED BEAMS

Let $\vec{A}_1$ and $\vec{A}_2$ be horizontally polarized waves whose wavevectors lie in the X-Y plane at angles θ_1 and $-\theta_2$ with respect to the X-axis:

$$\vec{A}_1 = \vec{i}A_1 \cos\theta_1 + \vec{j}A_1 \sin\theta_1$$

$$\vec{A}_2 = \vec{i}A_2 \cos\theta_2 - \vec{j}A_2 \sin\theta_2$$

$$A_1 = \alpha \exp[iwt + ik(y \cos\theta_1 - x \sin\theta_1)]$$

$$A_2 = \exp[iwt + i\phi + ik(y \cos\theta_2 - x \sin\theta_2)]$$

The intensity where these interfere is

$$I(x) = |\vec{A}_1 + \vec{A}_2|^2 = |\vec{A}_1|^2 + |\vec{A}_2|^2 + \vec{A}_1 \cdot \vec{A}_2 + A_1^* \cdot \vec{A}_2$$

$$= |A_1|^2 + |A_2|^2 + (A_1^* A_2 + A_1 A_2^*)(\cos\theta_1 \cos\theta_2 - \sin\theta_1 \sin\theta_2)$$

$$= 1 + \alpha^2 + 2\alpha \cos(\theta_1 + \theta_2) \cos[ky(\cos\theta_2 - \cos\theta_1)$$

$$+ kx(\sin\theta_2 + \sin\theta_1) + \phi]$$

$I(x)$ consists of an offset term and a spatial sinusoidal variation, the third term above. The visibility, γ, is

$$\gamma = \frac{I_{max} - I_{min}}{I_{max} + I_{min}} = \frac{2\alpha \cos(\theta_1 + \theta_2)}{1 + \alpha^2}$$

and is maximum for $\alpha = 1$ and $\theta_1 + \theta_2 = 0$. For the process interferometer used, $\alpha = 0.82$ and $\theta_1 + \theta_2 = 5°$, yielding $\gamma = 0.98$.

61

Appendix F

GRATING SKEW--DEPENDENCE ON MISALIGNMENTS BETWEEN TABLE ROTATION AXIS, INTERFEROMETER FRINGES, AND GRATING SURFACE

$\delta_x \equiv$ misalignment between grating surface and table rotation axis

$\delta_y \equiv$ misalignment between interferometer fringes and table rotation axis

$\theta \equiv$ angular displacement about table rotation axis between exposures

$R(n,\varphi) \equiv$ Matrix representing rotation by φ about n-axis.

The skew, ϵ, between the frequencies is obtained by rotating from the grating surface to the table rotation axis, then about the axis, and then back to the grating surface. The coordinates of a unit vector along the z-axis are thus transformed to show the skew

$$\begin{pmatrix} X \\ Y \\ Z \end{pmatrix} = R(1, -\delta_x) \, R(2, -\delta_y) \, R(3, \theta) \, R(2, \delta_y) \, R(1, \delta_x) \begin{pmatrix} 0 \\ 0 \\ 1 \end{pmatrix}$$

Assume

$$\cos \delta_x = \cos \delta_y = 1$$

$$\sin \delta_x = \delta_x$$

$$\sin \delta_y = \delta_y$$

so that

$$\begin{pmatrix} X \\ Y \\ Z \end{pmatrix} = \begin{pmatrix} 1 & 0 & 0 \\ 0 & 1 & -\delta_x \\ 0 & \delta_x & 1 \end{pmatrix} \begin{pmatrix} 1 & 0 & \delta_y \\ 0 & 1 & 0 \\ -\delta_y & 0 & 1 \end{pmatrix} \begin{pmatrix} \cos\theta & \sin\theta & 0 \\ -\sin\theta & \cos\theta & 0 \\ 0 & 0 & 1 \end{pmatrix}$$

$$\times \begin{pmatrix} 1 & 0 & -\delta_y \\ 0 & 1 & 0 \\ \delta_y & 0 & 1 \end{pmatrix} \begin{pmatrix} 1 & 0 & 0 \\ 0 & 1 & \delta_x \\ 0 & -\delta_x & 1 \end{pmatrix} \begin{pmatrix} 0 \\ 0 \\ 1 \end{pmatrix}$$

$$= \begin{pmatrix} -\delta_y \cos\theta + \delta_x \sin\theta + \delta_y \\ \delta_x \cos\theta - \delta_x \\ 1 \end{pmatrix}$$

retaining only first-order terms in δ_x and δ_y,

$$\epsilon = \sin\epsilon = \frac{X}{Z} \qquad .$$

$$= \delta_x \sin\theta + \delta_y (1 - \cos\theta)$$

Hence, the skew between frequencies has a first-order dependence on the alignment toleran-
ces δ_x and δ_y

	θ	$\sin\theta$	$1-\cos\theta$
Operational design	20°	0.34	0.06
Demonstration design	32°	0.53	0.15

Appendix G

FREQUENCY MEASUREMENT ERRORS

The determination of the grating frequencies and their ratio is done by performing a least-squares fit of the sine of measured diffraction angles to the grating equation, the independent variable being the order number.

If the incident angle is assumed to be zero, and

$$m = 1$$

then

$$\sin \theta = (\lambda/d)$$

Thus, a single measurement can yield a value for λ/d. The uncertainty in the computed value of grating frequency f due to theodolite resolution (theodolite aperture = D) is

$$\sigma_f = \delta\left(\frac{1}{d}\right) = \delta\left(\frac{\sin \theta}{\lambda}\right) = \frac{\cos \theta}{\lambda}\delta\theta$$

$$= \frac{\cos \theta}{\lambda}\left(\frac{\lambda}{D}\right) \approx \frac{1}{D}$$

$$\frac{\sigma_f}{f} \approx \frac{d}{D} = \frac{5 \times 10^{-6} \text{ m}}{50 \times 10^{-3} \text{ m}} = 1.0 \times 10^{-4}$$

The resulting error in the computed frequency ratio can be obtained by straightforward propagation of errors:

$$\frac{\sigma_{f_2/f_1}}{(f_2/f_1)} = \sqrt{2}\,\frac{\sigma_f}{f} = 1.4 \times 10^{-4}$$

64

By measuring many grating orders and computing the frequency from the slope of the least squares fit of the grating equation to the data, a more accurate estimate of the frequency (and frequency ratio) is possible. The expression for standard deviation of the slope, σ_s of a best-fit line is given by

$$\sigma_s^2 = \frac{1}{\sum \left(\frac{x_i}{\sigma_i}\right)^2} = \sigma_y^2 \frac{1}{\sum x_i^2}$$

when the X_i are measured so that their mean is zero. Since the X_i are the order numbers, this simply means measuring diffracted orders from -N to +N. Replacing the finite series with its closed form equivalent

$$\sigma_s^2 = \sigma_y^2 \frac{6}{2N(N+1)(2N+1)}$$

The practical upper limit of N is 10, yielding

$$\sigma_s = 0.036 \sigma_y$$

Thus, in principle, it is possible to determine the frequency ratio to an accuracy of 5 parts in 10^6

$$(0.036) \times 1.4 \times 10^{-4} = 5.0 \times 10^{-6}$$

Appendix H

COMPOUND GRATING EQUATIONS WITH SKEW BETWEEN COMPONENTS

In three dimensions, diffraction from a plane grating is governed by the equations

$$\sin \theta_i + \sin \theta_m = m\lambda/d$$

$$\sin \phi_i + \sin \phi_d = 0$$

where θ_i = angle between incident ray and a vertical plane perpendicular to grating surface (grating lines vertical)

ϕ_i = angle between incident ray and horizontal plane perpendicular to grating surface

θ_m, ϕ_d = corresponding angles for diffracted ray

By considering all rays as unit vectors, their components along the X and Y axes can be substituted into the equation since

$$X = \sin \theta_i$$

$$Y = \sin \phi_i$$

Hence

$$X_i + X_m = m\lambda/d$$

$$Y_i + Y_m = 0$$

These coordinates are chosen because they are conveniently transformed from the coordinate frame of one grating to that of the second.

Let

α = angular skew between gratings

Then, the diffraction of an incident ray (X_iY_i) from grating 1 yields

$$\begin{pmatrix} X_1 \\ \\ Y_1 \end{pmatrix} = \begin{pmatrix} \frac{m_1\lambda}{d_i} - X_i \\ \\ - Y_1 \end{pmatrix}$$

Rotating to second grating

$$\begin{pmatrix} X_1' \\ \\ Y_1' \end{pmatrix} = \begin{pmatrix} \cos\alpha & \sin\alpha \\ \\ -\sin\alpha & \cos\alpha \end{pmatrix} \begin{pmatrix} X_1 \\ \\ Y_1 \end{pmatrix}$$

Diffracting from the second grating

$$\begin{pmatrix} X_1 \\ \\ Y_2 \end{pmatrix} = \begin{pmatrix} \frac{m_2\lambda}{d_2} + X_1' \\ \\ + Y_1' \end{pmatrix}$$

Rotating back to the original coordinate frame

$$\begin{pmatrix} X_2' \\ \\ Y_1' \end{pmatrix} = \begin{pmatrix} \cos\alpha & \sin\alpha \\ \\ \sin\alpha & \cos\alpha \end{pmatrix} \begin{pmatrix} X_1 \\ \\ Y_2 \end{pmatrix}$$

Performing all of the above substitutions yields

$$\begin{pmatrix} X_2' \\ \\ Y_2' \end{pmatrix} = \begin{pmatrix} \frac{m_1\lambda}{d_1} + \frac{m_2\lambda}{d_2}\cos\alpha - X \\ \\ \frac{m_2\lambda}{d_2}\sin\alpha - Y_i\cos(2\alpha) \end{pmatrix}$$

In terms of the angles of incidence and diffraction,

$$\begin{pmatrix} \sin\theta_{m_1 m_2} \\ \\ \sin\phi_{m_1 m_2} \end{pmatrix} = \begin{pmatrix} \dfrac{m_1\lambda}{d_1} + \dfrac{m_2\lambda}{d_2}\cos\alpha - \sin\theta_i \\ \\ \dfrac{m_2\lambda}{d_2}\sin\alpha - \sin\phi_i\cos(2\alpha) \end{pmatrix}$$

which can be rewritten

$$\sin\theta_i + \sin\theta_{m_1 m_2} = \frac{m_1\lambda}{d_1} + \frac{m_2\lambda}{d_2}\cos\alpha$$

$$\sin\phi_i + \cos(2\alpha) + \sin\phi_{m_1 m_2} = \frac{m_2\lambda}{d_2}\sin\alpha$$

Compound Skewed Grating Equations and the GBC

First IR diffraction

$$\begin{pmatrix} X_{m_1 m_2} \\ \\ Y_{m_1 m_2} \end{pmatrix} = \begin{pmatrix} \dfrac{m_1\lambda}{d_1} + \dfrac{m_2\lambda}{d_2}\cos\alpha - X_i \\ \\ \dfrac{m_2\lambda}{d_2}\sin\alpha - Y_i\cos(2\alpha) \end{pmatrix}$$

Second IR diffraction after return from corner cube:

$$\begin{pmatrix} X_{mn} \\ \\ Y_{mn} \end{pmatrix} = \begin{pmatrix} \dfrac{n_1\lambda}{d_1} + \dfrac{n_2\lambda}{d_2}\cos\alpha - \left\{\dfrac{m_1\lambda}{d_1} + \dfrac{m_2\lambda}{d_2}\cos\alpha - X_i\right\} \\ \\ \dfrac{n_2\lambda}{d_2}\sin\alpha - \cos(2\alpha)\left\{\dfrac{m_2\lambda}{d_2}\sin\alpha - Y_i\cos(2\alpha)\right\} \end{pmatrix}$$

$$= \begin{pmatrix} \dfrac{n_1\lambda}{d_1} + \dfrac{n_2\lambda}{d_2}\cos\alpha - \dfrac{m_1\lambda}{d_1} - \dfrac{m_2\lambda}{d_2}\cos\alpha + X_i \\ \\ \dfrac{n_2\lambda}{d_2}\sin\alpha - \dfrac{m_2\lambda}{d_2}\cos(2\alpha)\sin\alpha + \cos^2(2\alpha)\,Y_i \end{pmatrix}$$

UV diffraction [input ray at $(-X_i, -Y_i)$]

$$\begin{pmatrix} X_{P_1P_2} \\ \\ Y_{P_1P_2} \end{pmatrix} = \begin{pmatrix} \dfrac{P_1\lambda}{d_1} + \dfrac{P_2\lambda}{d_2} \cos \alpha - (-X_i) \\ \\ \dfrac{P_2\lambda}{d_2} \sin \alpha + Y_i \cos (2\alpha) \end{pmatrix}$$

From inspection of the last two equations, it is apparent that the coefficients of Y_i in the second component are not identically the same unless $\alpha = 0$. Hence, the GBC requires that there be no skew between the gratings.

ABBREVIATIONS AND ACRONYMS

GBC   Grating Beam Combiner

HEL   High-energy laser

IR   Infrared

LODE   Large Optics Demonstration Experiment

OPD   Optical path difference

QWOT   Quarter-wave optical thickness

SEM   Scanning electron microscope

TOCS   Total Optical Control System

UV   Ultraviolet

DISTRIBUTION LIST

James W. Cusack   6
RADC/OCSE

RADC/TSLD   1   2
GRIFFISS AFB NY 13441

RADC/DAP   2   3
GRIFFISS AFB NY 13441

ADMINISTRATOR   12   5
DEF TECH INF CTR
ATTN: DTIC-DDA
CAMERON STA BG 5
ALEXANDRIA VA 22314

Itek Corp   5   3
10 Maguire Rd

Lexington MA 02173

AFWL/ARAA   1   4
Dr. R. Shagam
Kirtland AFB, NM 87117

AFWL/ARAA   1   5
Attn: Dr. J. Fender
Kirtland AFB, NM 87117

The Aerospace Corp Attn: Dr. E.W. Silvertooth Bldg 110 MS 2339 PO Box 92957 Los Angeles, CA 90009	1	6
The Aerospace Corp Attn: T. Taylor Bldg 115 Room 1334C PO Box 92957 Los Angeles, CA 90009	1	7
Analytic Decisions Inc Attn: Emmanuel Goldstein 1401 Wilson Blvd Arlington, VA 22209	1	8
BDM Corp Attn: K. Probst 1820 Randolph Rd Albuquerque NM 87106	1	9
BMD/ATC Attn: A. Carmichael PO Box 1500 Huntsville, AL 35807	1	10
Boeing Aerospace Co. Attn: B. Allasina PO Box 3999 Seattle, WA 98124	1	11
Charles Starke Draper Labs Attn: Dr. J. Negro 555 Technology Dr. Cambridge, MA 02139	1	12

Charles Starke Draper Labs   1   13
Attn: Dr. Keto Soosar
555 Technology Dr
MS 95
Cambridge, MA 02139

DARPA/DEO   1   14
Attn: Col Ronald Prater
Arlington, VA 22209

Eastman Kodak   1   15
Attn: Robert Keim
Kodak Aparatus Division
121 Lincoln Ave.
Rochester, NY 14650

Eastman Kodak   1   16
Attn: Richard Price
KAD-Lincoln Park
901 Elmgrove RD
Rochester, NY 14650

GRC   1   17
Attn: G. Gurski
7655 Old Springhouse RD
McLean, VA 22102

Hughes Aircraft   1   18
Attn: Martin Flannery
MS D/125 Bldg 6
Centenela & Teal Sts
Culver City, CA 90230

Hughes Aircraft   1   19
Attn: R. Auelmann

Centenela & Teal Sts
Culver City, CA 90230

Itek Corp   1   20
Attn: Roland Plante
Optical Systems Division
10 Maguire Rd.
3251 Hanover St.
Palo Alto, CA 94304

Lockheed Space and Missile Co.   1   22
Attn: Dennis Aspinwall
Dept 5203 Bldg. 201
3251 Hanover St.
Palo Alto, CA 94304

Lockheed Space and Missile Co.   1   23
Attn: Dick Wallner
Dept 5203 Bldg 201
3251 Hanover St.
Palo Alto, CA 94304

Martin Marietta Aerospace   24
Attn: C.W. Spieth
Denver Division
PO Box 179
Denver, CO 80201

MIT/Lincoln Laboratory   1   25
Attn: Alex Parker
PO Box 73
Lexington, MA 02173

MRJ Corp   1   26
Attn: Dr. Kenneth Robinson
71 Blake St.
Needham, MA 02192

NASA Ames   1   27
Attn: James Murphy
MS 244-7
Moffett Field, CA 94035

NASA Marshall Space Flight Center   1   28
Attn: Charles O. Jones
Mail Code EC32
Huntsville, AL 35812

Naval Sea Systems Command   1   29
Attn: Dr. Sadeg Siahatgar
PMS-405
NC 1 Room 11N08
Washington, DC 20742

Naval Weapons Center Attn: Dr. H. Bennett Code 6018 China Lake , CA 93555	1	30
Perkin Elmer Attn: Dr. David Dean MS 241 Main Ave Norwalk, CT 06856	1	31
Perkin Elmer Attn: Henry Dieselmen 100 Wooster Heights Rd. Danbury, CT 06810	1	32
Rockwell International Attn: R. Greenberg Space Division 12214 Lakewood Blvd Downey, CA 90241	1	33
Riverside Research Institute DARPA Laser Library 1701 N Fort Myer Dr. Suite 711 Arlington, VA 22209	1	34
SD/YNS Attn: Col H.A. Shelton PO Box 92960 Worldway Postal Center Los Angeles, CA 90009	1	35
United Technologies Research Center Attn: Dr. J. Pearson Optics & Applied Technology Lab PO Box 2691 West Palm Beach, FL 33402	1	36
University of Arizona Attn: Prof Robert Shannon %Charles Peyton Administration Bldg Tuscon, AZ 85721	1	37

W.J. Schaffer Assoc. Inc.   1   38
Attn: Edward Borsare
10 Lakeside Office Park
Wakefield, MA 01880

United Technologies Research Center   1   39
Attn: A. Angelbeck
East Hartford CT 06108

W.J. Schaffer Assoc. Inc. 1 38
Attn: Edward Borsare
10 Lakeside Office Park
Wakefield, MA 01880

United Technologies Research Center 1 39
Attn: A. Angelbeck
East Hartford CT 06108

MISSION
of
Rome Air Development Center

RADC plans and executes research, development, test and selected acquisition programs in support of Command, Control Communications and Intelligence (C^3I) activities. Technical and engineering support within areas of technical competence is provided to ESD Program Offices (POs) and other ESD elements. The principal technical mission areas are communications, electromagnetic guidance and control, surveillance of ground and aerospace objects, intelligence data collection and handling, information system technology, ionospheric propagation, solid state sciences, microwave physics and electronic reliability, maintainability and compatibility.